

Development of control systems of optical beam profile for optical tweezer arrays

submitted by

Aditya Tripathi

(Roll No. P0191302)

Under the Guidance of

Dr. Takeshi Fukuhara



submitted to

Department of Physical Sciences

**University of Mumbai-Department of Atomic Energy Center
for Excellence in Basic Science**

Mumbai - 400098, India

December 2023



RIKEN Center for Quantum Computing

2-1 Hirosawa, Wako, Saitama, 351-0198, Japan

Tel: +81-48-462-1111

Fax: +81-48-462-1403

<https://rqc.riken.jp/en/>



December 15, 2023

To whom it may concern,

This is to certify that CEBS student Aditya Tripathi has undertaken project work from June 23rd 2023 to December 22nd 2023 in my lab at RIKEN.

This submitted project report titled "Development of control systems of optical beam profile for optical tweezer arrays" is towards the academic requirements of the M.Sc. Thesis Project Course at UM-DAE CEBS.

Sincerely yours,

A handwritten signature in blue ink, appearing to read 'Takeshi Fukuhara'.

Dr. Takeshi Fukuhara

Team Leader

RIKEN Center for Quantum Computing

Acknowledgements

I take this opportunity to acknowledge and express my gratitude to all those who supported and guided me during my project work. Firstly, I extend my sincere gratitude to Prof. Takeshi Fukuhara for being an amazing and supportive supervisor, and also for being kind enough to provide me with an opportunity to pursue an experimental project in his lab. Without his guidance, this project would not have been possible.

Using the optical table and related instruments for the first time could have been daunting if it were not for the support of Yamamoto-san and Ozawa-san. I would like to thank Dr. Yamamoto and Dr. Ozawa, for their constant help and guidance and also for answering my every little experimental or theory-related query.

Moving to a new country can be very difficult thus I would like to thank Kizaki-san for helping me settle in Japan.

I would also like to thank Daniel for the scientific discussions we had related to lasers and applied physics. I would like to thank Sandeep, Rahul, and Li for their support and motivation.

I thank my friends at CEBS for motivating and helping me out whenever I needed their help. I would also like to thank my mother for her unwavering support.

Contents

[Acknowledgements](#)

[Contents](#)

[List of Figures](#)

[Abbreviations](#)

1	Introduction	1
1.1	Background and Motivation	1
1.2	Project Overview	1
1.3	Significance	2
2	Theoretical Estimations	5
2.1	Introduction	5
2.2	Oscillator Model for Dipole Potential	6
2.2.1	The interaction of driving field and induced dipole	6
2.2.2	The Force and the Scattering Rate	7
2.3	Polarizability	7
2.4	The Dipole Potential and Scattering Rate	9
2.5	Multi-Level Atoms	9
2.6	For Sr atoms	10
2.6.1	Plots of U_{dip} and Γ_{sc} versus Wavelength	11
2.7	Summary	14
3	Gaussian Beam	15
3.1	Introduction	15
3.2	Gaussian Mode	15
3.3	M squared parameter	20
3.3.1	Observations	20
3.4	The Ray Transfer Matrix Method	21
3.5	Summary of Fiber Optic Physics	24

Contents

3.5.1	Polarization Maintaining Fiber	24
3.5.2	Mode Field Diameter	25
4	Acousto Optic Modulator and PID stabilization setup	27
4.1	Introduction	27
4.2	Acousto Optic Modulator	28
4.2.1	Theory	28
4.2.2	Signal Mixer and Amplifier	29
4.2.3	Diffraction Efficiency	31
4.3	The Optical Setup:	32
4.4	PID (Proportional-Integral-Derivative)	34
4.4.1	Theory:	34
4.4.2	Implementation:	37
4.4.3	Results:	38
5	Acousto-Optic Deflector and High-Frequency Generation using Direct Digital Synthesis	41
5.1	Introduction	41
5.2	Characteristics of Acousto-Optic Deflector	42
5.3	Direct Digital Synthesis using AD9959	44
5.3.1	Theory of Operation:	45
5.3.2	Using AD9959 Eval Board with Raspberry Pi Pico	47
5.4	Optical Setup	49
5.5	Using DDS with AOD	50
5.6	Stabilizing the Laser Power Output	50
6	Results and Future Prospects	53
6.1	Summary:	53
6.2	1-d Traps:	53
6.3	2-d Traps:	55
6.4	Conclusions and Future Prospectives:	57
A	Light Matter Interaction and Laser Cooling Techniques	59
A.0.1	Light Matter Interaction	59
A.0.2	Laser Cooling Techniques	60
B	Optical Elements Description	65
B.1	Half-Wave Plate	65
B.2	Action of a Quarter-Wave Plate	66
B.3	Interaction with a Polarizing Beam Splitter	66
B.4	Ray Transfer Matrix of a Thin Lens	67

Bibliography	69
---------------------	-----------

List of Figures

2.1	Level Scheme of Strontium HANLEY (2018)	11
2.2	Plot of Dipole Potential versus Wavelength	12
2.3	Plot of Scattering Rate versus Wavelength	13
3.1	Gaussian Laser Profile in between the optical setup, as seen from the Camera. The above fit is for the x direction and below one is for the y direction (the interference pattern is due to misaligned optics)	16
3.2	Gaussian Beam profile cross-section showing the variation of beam spot $w(z)$ Wiki	19
3.3	Rectangular Transverse Modes ($TEM(mn)$) (Wikipedia)	19
3.4	M^2 fit in the x-direction	21
3.5	M^2 fit in the y-direction	22
3.6	A ray vector being transformed by an optical element	23
4.1	A rough sketch of AOM	29
4.2	RF Mixer	30
4.3	RF Mixer Characteristic Curve	30
4.4	Diffraction Efficiency Curve	32
4.5	Optical Setup	33
4.6	PID Block Diagram	34
4.7	QNimble PID Flowchart	36
4.8	Ziegler-Nichols Method Ellis (2012)	37
4.9	Output from photodiodes without PID and constant power input in AOM (top one is PD1 output and bottom one is the PD2 output)	39
4.10	Output from photodiodes with PID stabilization (top one is PD1 output and bottom one is the PD2 output)	40
5.1	Diffraction Efficiency vs Frequency from Datasheet	43
5.2	Diffraction Efficiency versus Frequency	44
5.3	Diffraction Angle versus Frequency in MHz	45
5.4	Flowchart for DDS Analog Devices	45
5.5	DDS flowchart with Phase Accumulator Analog Devices	46

List of Figures

5.6	Block wiring diagram for DDS with RPi Pico (The current drawn by Analog Circuitry of DDS is roughly 0.2 A, when in operation, therefore additional power supply is recommended). More information about the schematic can be found in Huegler and Meyer (2023)	48
5.7	Optical Setup with AOD in place	49
5.8	DDS RF Output Amplitude vs Frequency	50
5.9	Plot of 1st Diffracted Beam Power for different Frequencies and Amplitude (the amplitude tuning words have been scaled to values from 0 to 1)	51
5.10	Contour Plot for Constant Power Output	52
6.1	Six frequencies fast switch output. Exposure time for the first image is 6ms and that for the second one is 12ms	54
6.2	Cross-Section for figure 6.1	54
6.3	Output from PD3 (figure 5.7), the two plots were taken 25 minutes apart	55
6.4	Random 1-d Pattern	56
6.5	Some 2-d Patterns generated after the Second AOD	56
6.6	Optical Setup to generate 2-d Patterns	57
A.1	Magneto Optical Trap Setup Foot (2005)	63

Abbreviations

ADC	Analog to Digital Converter
AOM	Acousto Optic Modulator
AOD	Acousto Optic Deflector
DAC	Digital to Analog Converter
DDS	Direct Digital Synthesis
FPGA	Field Programmable Gate Arrays
IF	Intermediate Frequency
LO	Local Oscillator
MFD	Mode Field Diameter
MOT	Magneto-Optical Trap
PBS	Polarizing Beam Splitter
RF	Radio Frequency
RPi	Raspberry Pi
RTM	Ray Transfer Matrix
SPI	Serial Peripheral Interface
TEM	Transverse Electromagnetic Mode

Chapter 1

Introduction

1.1 Background and Motivation

The field of atomic physics and quantum optics has seen remarkable advancements in recent years, particularly in the manipulation and control of individual atoms and photons. It has been shown ([Barredo et al. \(2016\)](#)) that an arbitrary, fully loaded, two-dimensional array of a single atom can be made using fast response acousto-optic devices. Thus this project aims to build a control system for Strontium atom-based atomic tweezers.

1.2 Project Overview

This project is structured into several chapters, starting from the theoretical derivations for estimating different parameters required for trapping Strontium atoms, proceeding to describe the optical setup and different acousto-optic elements used in the project. The report ends by describing results and discussing the future scope of improvements and future prospects.

- **Theoretical Estimations:** This section provides a foundational understanding of the interaction between the driving field and induced dipole, detailing the oscillator model and deriving the dipole potential and scattering rates in multi-level atoms, with a specific focus on Strontium atoms.
- **Gaussian Beam:** A detailed exploration of the Gaussian beam mode, its characteristics, and its role in atomic trapping. This includes an examination of the M squared parameter and the Ray Transfer Matrix Method.
- **Acousto Optic Modulator and PID Stabilization Setup:** Here, we delve into the theory and application of Acousto Optic Modulators, their role in stabilizing the intensity of laser beams, and the integration of PID (Proportional-Integral-Derivative) controllers for maintaining the stability beam intensity.
- **Acousto-Optic Deflector and High-Frequency Generation:** This chapter discusses the characteristics of Acousto-Optic Deflectors and the use of Direct Digital Synthesis for high-frequency generation, crucial for precise control of laser beam angle in optical setups.
- **Results and Future Prospects:** The project culminates with a summary of the results obtained, the practical realization of one- and two-dimensional traps, and a discussion on their robustness and future prospects.

1.3 Significance

This project aims to understand atomic manipulation using optical methods, a field that stands at the forefront of modern quantum technologies. Recently it was also shown ([Huegler et al. \(2023\)](#)) that a logical quantum processor can be made using reconfigurable atom arrays. The insights gained from this project may be used

for the development of quantum computing architecture, high-precision measuring devices, and the study of fundamental quantum phenomena.

Chapter 2

Theoretical Estimations

2.1 Introduction

The intensity gradient of the laser light creates a dipole force acting on an atom. This force is conservative in nature, thus we can attribute a potential to this force. This dipole potential is due to the polarization of the atom in the laser field. The atoms can be trapped in the minima of this potential for the red-detuned case or in the valley of 2 maxima for the blue-detuned case. The light-atom interaction also leads to the scattering of photons, therefore one also needs the expression or the scattering rate which sets a limit on the performance of dipole atom traps. The treatment in this chapter will be semi-classical. The atom is assumed as a simple oscillator subjected to a classical radiation field. The primary reference for these derivations can be found in [Grimm et al. \(2000\)](#).

2.2 Oscillator Model for Dipole Potential

2.2.1 The interaction of driving field and induced dipole

The electric field \mathbf{E} of the laser induces a dipole moment \mathbf{p} that oscillates at the driving frequency. The interaction potential of the induced dipole moment \mathbf{p} is given by

$$U_{dip} = -\frac{1}{2}\langle \mathbf{p}\mathbf{E} \rangle \quad (\text{Grimmet al., 2000}) \quad (2.1)$$

The half factor comes from the fact that the dipole moment is induced and not permanent. This can be seen in the following way. The force on a dipole is given by $\vec{\mathbf{F}} = (\vec{\mathbf{p}} \cdot \nabla) \vec{\mathbf{E}}$. Now if we take the case of permanent dipole moment this expression can be written as $\nabla(\vec{\mathbf{p}} \cdot \vec{\mathbf{E}})$, because the gradient of the permanent dipole moment is 0. However, if the dipole moment is induced ($p = \alpha E$) (α depends on the driving frequency) then,

$$\begin{aligned} (\vec{\mathbf{p}} \cdot \nabla) \vec{\mathbf{E}} &= \nabla(\vec{\mathbf{p}} \cdot \vec{\mathbf{E}}) - \vec{\mathbf{E}} \cdot (\nabla \vec{\mathbf{p}}) = \nabla(\alpha |\vec{\mathbf{E}}|^2) - \alpha \vec{\mathbf{E}} \cdot (\nabla \vec{\mathbf{E}}) \\ &= \frac{1}{2} \nabla(\alpha |\vec{\mathbf{E}}|^2) = \frac{1}{2} \nabla(\vec{\mathbf{p}} \cdot \vec{\mathbf{E}}). \end{aligned}$$

The integral of this gives the potential. The potential in 2.1 is averaged over time in the angular brackets to get rid of fast-moving terms of the electric field. Taking the complex notation of $\mathbf{E}(\mathbf{r}, t) = \hat{e}\tilde{E}(\mathbf{r})e^{-i\omega t} + c.c.$ and $\mathbf{p}(\mathbf{r}, t) = \hat{e}\tilde{p}(\mathbf{r})e^{-i\omega t} + c.c.$ and $\tilde{p} = \alpha \tilde{E}$

$$\langle \mathbf{p}\mathbf{E} \rangle = |\tilde{E}|^2(\alpha + \alpha^*) = 2|\tilde{E}|^2 \operatorname{Re}(\alpha)$$

Therefore,

$$U_{dip} = -\frac{1}{2\epsilon_0 c} \operatorname{Re}(\alpha) I \quad (2.2)$$

where $I = 2\epsilon_0 c |\tilde{E}|^2$, now we just need to calculate α .

2.2.2 The Force and the Scattering Rate

The force on the atom can be calculated by taking the gradient of the dipole potential,

$$\mathbf{F}_{\text{dip}}(\mathbf{r}) = -\nabla U_{\text{dip}}(\mathbf{r}) = \frac{1}{2\epsilon_0 c} \text{Re}(\alpha) \nabla I(\mathbf{r}) \quad (2.3)$$

The power absorbed is given by,

$$P_{\text{abs}} = \langle \dot{\mathbf{p}} \cdot \mathbf{E} \rangle = 2\omega \text{Im} \left(\tilde{p} \tilde{E}^* \right) = \frac{\omega}{\epsilon_0 c} \text{Im}(\alpha) I$$

This can be calculated using the complex notation as mentioned earlier and then taking the time average of the dot product. The power absorbed is released as spontaneous emission, thus we can say that the absorbed photon is scattered. We find the scattering rate as,

$$\Gamma_{\text{sc}}(\mathbf{r}) = \frac{P_{\text{abs}}}{\hbar\omega} = \frac{1}{\hbar\epsilon_0 c} \text{Im}(\alpha) I(\mathbf{r}) \quad (2.4)$$

2.3 Polarizability

Classical calculations of polarizability involve considering Lorentz's model of a classical oscillator. The equation of motion for the same is,

$$\ddot{x} + \Gamma_\omega \dot{x} + \omega_0^2 x = -eE(t)/m_e$$

Using the ansatz $e^{-i\omega t}$ (ω being the frequency of the oscillating electric field) one gets,

$$\vec{x}(t) = \frac{e\vec{E}(t)}{m(\omega^2 + i\omega\Gamma_\omega - \omega_0^2)}$$

and because $\tilde{p} = -e\tilde{x} = \alpha\tilde{E}$ we get,

$$\alpha = \frac{e^2}{m_e} \frac{1}{\omega_0^2 - i\omega\Gamma_\omega - \omega^2} = 6\pi\epsilon_0 c^3 \frac{\Gamma_\omega}{\omega^2} \frac{1}{\omega_0^2 - i\omega\Gamma_\omega - \omega^2} \quad (2.5)$$

where Γ_ω is,

$$\Gamma_\omega = \frac{e^2\omega^2}{6\pi\epsilon_0 m_e c^3}$$

The expression for Γ_ω can be derived from the classical theory of radiation damping.

The real and imaginary parts of α are,

$$Re(\alpha) = 6\pi\epsilon_0 c^3 \frac{\Gamma}{\omega_0^2} \frac{\omega_0^2 - \omega^2}{(\omega_0^2 - \omega^2)^2 + \omega^2\Gamma_\omega^2} = 6\pi\epsilon_0 c^3 \frac{\Gamma}{2\omega_0^3} \left(\frac{1}{\omega_0 + \omega} + \frac{1}{\omega_0 - \omega} \right),$$

$$Im(\alpha) = 6\pi\epsilon_0 c^3 \frac{\Gamma}{\omega_0^2} \frac{\omega\Gamma_\omega}{(\omega_0^2 - \omega^2)^2 + \omega^2\Gamma_\omega^2} = \frac{3\pi\epsilon_0 c^3}{\omega_0} \left(\frac{\Gamma}{\omega_0 + \omega} + \frac{\Gamma}{\omega_0 - \omega} \right)^2.$$

Here $\Gamma = \Gamma_\omega(\omega_0/\omega)^2$ is the on-resonance damping rate. This is the linewidth one gets in the measurements of the spectra of the atom (barring the factor of 2π which converts it into the convenient unit of Hz). And the approximation $|\Gamma_\omega/(\omega_0 - \omega)| \ll 1$ has been used. One important difference between quantum mechanical and classical oscillators is the possible case of saturation at high intensities (Grimm et al. (2000)). But in dipole trapping we use far detuned light and low saturation.

Thus we can use the above expressions.

2.4 The Dipole Potential and Scattering Rate

Using the above values of α and equations (2.2) and (2.4) we get the main formulas,

$$U_{dip}(\vec{r}) = -\frac{3\pi c^2}{2\omega_0^3} \left(\frac{\Gamma}{\omega_0 + \omega} + \frac{\Gamma}{\omega_0 - \omega} \right) I(\vec{r}), \quad (2.6)$$

$$\Gamma_{sc}(\vec{r}) = \frac{3\pi c^2}{2\hbar\omega_0^3} \left(\frac{\omega}{\omega_0} \right)^3 \left(\frac{\Gamma}{\omega_0 + \omega} + \frac{\Gamma}{\omega_0 - \omega} \right)^2 I(\vec{r}). \quad (2.7)$$

The dipole potential gives the trap depth. The scattering rate should be low to avoid heating. Thus for optimum performance, the intensity can be evaluated and that can be used to calculate the laser power or vice versa.

2.5 Multi-Level Atoms

In general different atoms have a complex electronic level structure. The same is the case with strontium atoms. In such a case if a far-detuned laser light is used we employ second-order perturbation theory. The reason why the first order vanishes is that the diagonal matrix elements of the induced dipole Hamiltonian are 0. The second-order energy shift in the ground state for a perturbing Hamiltonian $H_1 = -\vec{\mu} \cdot \vec{E}$ is given by,

$$\Delta E_{gnd}^2 = \sum_{j \neq gnd} \frac{|\langle j | H_1 | gnd \rangle|^2}{E_{gnd} - E_j} \quad (2.8)$$

where the superscript 2 implies second order. Later, for strontium atoms, the summation will have only two terms. Using 2.8 and $\vec{E} = \vec{\mathcal{E}} e^{-i\omega t} + c.c$ we get,

$$\Delta E = \sum_{j \neq i} \frac{|\langle j | \mu | i \rangle|^2 \mathcal{E}^2}{E_i - E_j}. \quad (2.9)$$

In the above gnd (ground) has been replaced by i for generality. Next, we use the damping coefficient,

$$\Gamma_{ij} = \frac{\omega_0^3}{3\pi\epsilon_0\hbar c^3} |\langle j|\mu|i\rangle|^2$$

Using this we know the dipole transition matrix elements in terms of damping rate which can be measured experimentally. Using this 2.9 becomes,

$$\Delta E_i = \frac{3\pi c^2}{2\omega_0^3} \sum_{j \neq i} \frac{\Gamma_{ij}}{(\omega_i - \omega_j)} I(\vec{r}), \quad (2.10)$$

where $E_i = \hbar\omega_i$ and $I = 2\epsilon_0 c^2 \mathcal{E}^2$.

2.6 For Sr atoms

Strontium is a divalent atom and there are two relevant (have the largest linewidth) transitions from 1S_0 state to 1P_1 and 3P_1 (See figure 2.1). The 3P_1 transition is forbidden, but is weakly allowed due to state mixing Boyd (2007).

Using the semiclassical approach the formula for the dipole potential and scattering rate will be modified because now we take the model to have two excitation levels. Equation 2.6 and 2.7 becomes,

$$U_{dip}(\vec{r}) = -\frac{3\pi c^2}{2} \left[\left(\frac{\Gamma_1}{\omega_{01} + \omega} + \frac{\Gamma_1}{\omega_{01} - \omega} \right) \frac{1}{\omega_{01}^3} + \left(\frac{\Gamma_2}{\omega_{02} + \omega} + \frac{\Gamma_2}{\omega_{02} - \omega} \right) \frac{1}{\omega_{02}^3} \right] I(\vec{r}) \quad (2.11)$$

$$\Gamma_{sc}(\vec{r}) = \frac{3\pi c^2 \omega^3}{2\hbar} \left[\left(\frac{\Gamma_1}{\omega_{01} + \omega} + \frac{\Gamma_1}{\omega_{01} - \omega} \right)^2 \frac{1}{\omega_{01}^6} + \left(\frac{\Gamma_2}{\omega_{02} + \omega} + \frac{\Gamma_2}{\omega_{02} - \omega} \right)^2 \frac{1}{\omega_{02}^6} \right] I(\vec{r}) \quad (2.12)$$

where Γ_1 and Γ_2 are the line widths for $5s^2 {}^1S_0 \rightarrow 5s5p {}^1P_1$ and $5s^2 {}^1S_0 \rightarrow 5s5p {}^3P_1$, and ω_{0i} is the respective energy difference of the level divided by \hbar .

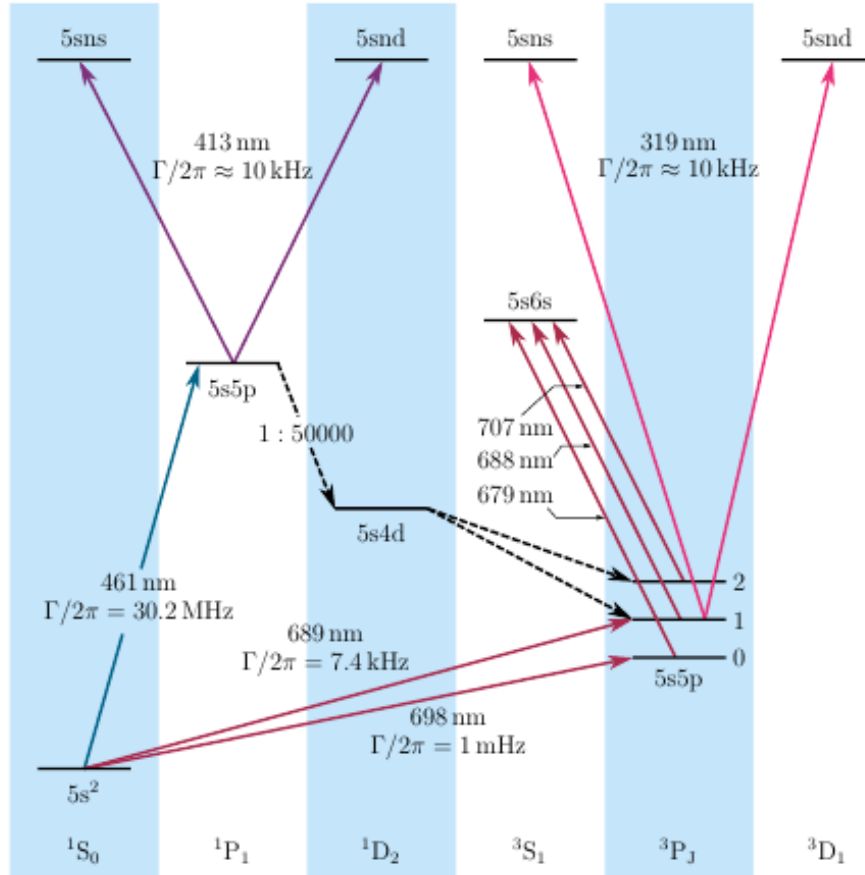


FIGURE 2.1: Level Scheme of Strontium HANLEY (2018)

2.6.1 Plots of U_{dip} and Γ_{sc} versus Wavelength

The wavelength dependence of the previously defined quantities is shown. To estimate them we should first find the intensity, to find intensity we first assume the power. We assume the power for a single trap to be 0.025W and the beam waist(w_0) for a Gaussian beam profile to be $1\mu\text{m}$ (beam waist is the radius of the laser profile at its minimum). The peak intensity is thus given by,

$$I = \frac{2P}{\pi w_0^2}.$$

The laser wavelength that is used is 813nm. This (wavelength) is the magic wavelength. At this wavelength, the AC stark shift is the same for both the levels, i.e. $\Delta E_{1S_0} = \Delta E_{3P_0}$ ([Takamoto and Katori \(2003\)](#)). This means that the clock transition frequency does not change. From the perspective of using Sr atoms as qubits, this is very useful. If eigenstates 1S_0 and 3P_0 are taken as the two levels of a qubit ($|0\rangle$ and $|1\rangle$), then we know that the time evolution of each level is given by $\exp(-iEt/\hbar)$, where ' E ' is the energy of that level. Thus the relative phase between the two levels depends on their energy difference. Using the 813 nm laser does not change the energy difference between 1S_0 and 3P_0 , hence preventing dephasing. At this wavelength the scattering rate is found to be $\approx 0.5\text{Hz}$ and the $\mathbf{U}_{\text{dip}}/\mathbf{k}_b \approx 1\text{mk}$

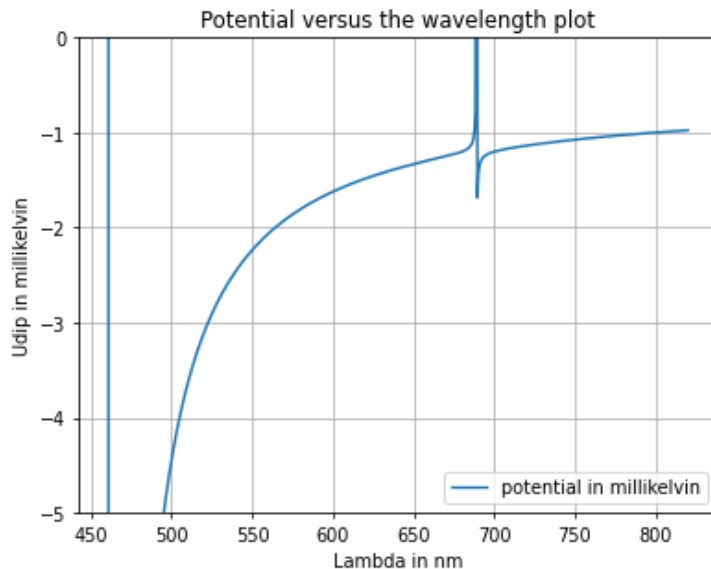


FIGURE 2.2: Plot of Dipole Potential versus Wavelength

In figure [2.2](#) and [2.3](#) we can see potential and scattering rate plotted against wavelength. In these figures, one can also see the singularity behavior near the resonance at 461nm and 689nm. Next, we find the trapping frequency for the above values of

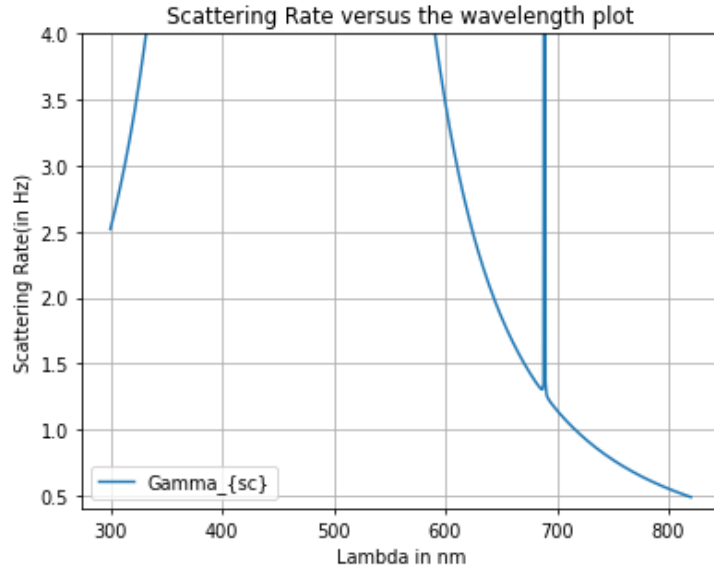


FIGURE 2.3: Plot of Scattering Rate versus Wavelength

power and beam waist. For a gaussian profile, the intensity is given by:

$$I(r, z) = \frac{2P}{\pi w_0^2} \exp\left(-2\frac{r^2}{w_0^2(z)}\right).$$

Taking the potential depth at ($r=0, z=0$) as \hat{U} and approximating the above beam profile for the potential depth, we get,

$$U(r, z) \approx -\hat{U} \left[1 - 2 \left(\frac{r}{\omega_0} \right)^2 - \left(\frac{z}{z_R} \right)^2 \right].$$

Thus in the radial and axial direction trapping frequencies respectively,

$$\omega_r = (4\hat{U}/m\omega_0^2)^{1/2}, \quad \omega_z = (2\hat{U}/mz_R^2)^{1/2}.$$

For the depth of 1mK and, $1\mu m$, and the mass of Sr atoms, we get the approximate values, where (z_R) is the Rayleigh length (more about this in the next chapter).

$$\omega_r \approx 600 \text{ kHz} ; \quad \omega_z \approx 100 \text{ kHz}$$

As expected in the radial direction the force is stronger because the beam waist is smaller than the Rayleigh length.

2.7 Summary

In this chapter, we found the theoretical estimates for the dipole potential and the scattering rate. For a single trap of power 25mW, beam waist of $1\mu m$ and wavelength 813nm, the potential depth was found to be around 1mK. This much trap depth is suitable for tweezer experiments. Next, we found the scattering rate which was around 0.5Hz, i.e. every two seconds a photon will be scattered from the atom. This is also good as the atom will not heat up.

Chapter 3

Gaussian Beam

3.1 Introduction

As mentioned in the previous chapter, a gaussian beam profile or the beam mode TEM_{00} is used to make atom traps. This chapter contains a heuristic derivation of the gaussian beam profile of the laser. Followed by the quality test experiment for the gaussian profile of the laser being used. Then there is a short description of the Ray-Transfer method, which helps in calculations when the beam passes through different optical equipment. In the end, there is a short description of the physics of fiber optic cable.

3.2 Gaussian Mode

The transverse electromagnetic mode 00 ($TEM00$) represents the fundamental mode of a laser resonator, characterized by its gaussian spatial intensity profile and its propensity to produce a highly collimated and symmetric beam. To heuristically

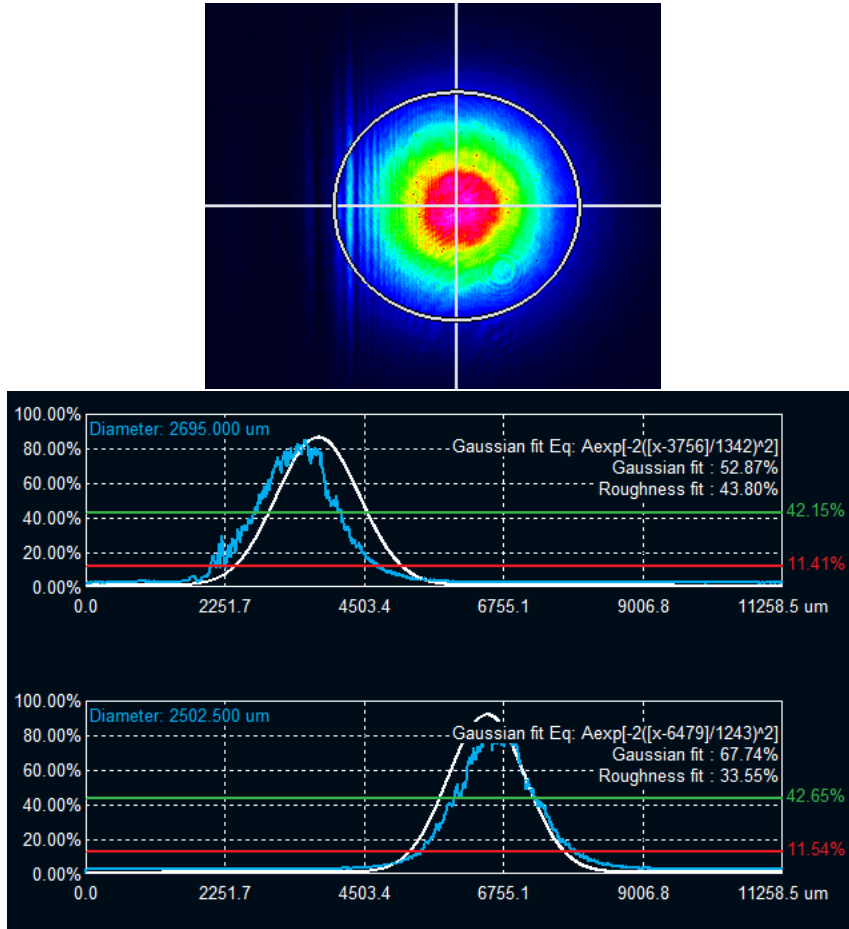


FIGURE 3.1: Gaussian Laser Profile in between the optical setup, as seen from the Camera. The above fit is for the x direction and below one is for the y direction (the interference pattern is due to misaligned optics)

derive it we start with the Helmholtz equation:

$$(\nabla^2 + k_0^2) \vec{E}(x, y, z) = 0. \quad (3.1)$$

We can simplify the above and take the polarization along the x direction. The purpose is to construct a beam that largely propagates in the z direction and decays quickly in the radial direction. Thus we make the paraxial approximation ($k_x, k_y \ll k_z$),

$$k_z = \sqrt{k_0^2 - k_x^2 - k_y^2} \approx k_0 \left(1 - \frac{k_x^2 + k_y^2}{2k_0^2} \right) \quad (3.2)$$

The required solution for the Helmholtz equation can be constructed by superimposing many plane waves with dominant k_z component.

$$E(x, y, z) = \int \int \tilde{E}(k_x, k_y) \exp(-i\mathbf{k} \cdot \mathbf{r}) dk_x dk_y \quad (3.3)$$

$$\begin{aligned} E(x, y, z) &= \int \int \tilde{E}(k_x, k_y) \exp \left[-ik_0 \left(1 - \frac{k_x^2 + k_y^2}{2k_0^2} \right) z - ik_x x - ik_y y \right] dk_x dk_y \\ \implies E(x, y, z) &= \int \int \tilde{E}(k_x, k_y) \exp \left[i \left(\frac{k_x^2 + k_y^2}{2k_0} \right) z - ik_x x - ik_y y \right] e^{-ik_0 z} dk_x dk_y \end{aligned} \quad (3.4)$$

It is also seen that $e^{ik_0 z} E(x, y, z) = \tilde{E}$ satisfies the paraxial wave equation given by,

$$2ik_0 \frac{\partial}{\partial z} \tilde{E}(x, y, z) = \left(\frac{\partial^2}{\partial x^2} + \frac{\partial^2}{\partial y^2} \right) \tilde{E}(x, y, z)$$

This is an important point. Traditionally one would make the paraxial approximation on the Helmholtz equation in this format and then derive the electric field equation. In principle, the paraxial wave equation mentioned above gives many solutions but here we are concerned with the most simple. Suppose the beam at $z=0$ is described by a gaussian:

$$E(x, y, 0) = E_0 \exp \left(-\frac{x^2 + y^2}{w_0^2} \right)$$

Substituting this in equation 3.4 and then inverting the fourier transform, we get,

$$\tilde{E}(k_x, k_y) = \frac{E_0 w_0^2}{4\pi} \exp \left(-\frac{w_0^2}{4} (k_x^2 + k_y^2) \right).$$

Now we can use this to find the field at any point in direction,

$$E(x, y, z) = \frac{E_0 w_0^2}{4\pi} \iint_{-\infty}^{\infty} dk_x dk_y \exp\left(-\frac{w_0^2}{4} [k_x^2 + k_y^2]\right) \cdot \exp(-i[k_x x + k_y y]) \exp\left(i \frac{[k_x^2 + k_y^2] z}{2k_0}\right) e^{-ik_0 z}.$$

which finally gives,

$$E(x, y, z) = \frac{E_0}{\sqrt{1 + (z/z_R)^2}} \exp\left(\frac{ik_0}{2\tilde{q}} (x^2 + y^2)\right) \exp(i [k_0 z - \psi]) \quad (3.5)$$

where,

$$\tilde{q} = z - iz_R, \quad z_R = \frac{k_0 w_0^2}{2} = \frac{\pi w_0^2}{\lambda}, \quad \tan(\psi) = z/z_R$$

and

$$w(z) = w_0 \sqrt{1 + (z/z_R)^2}$$

$w(z)$ is the beam radius at distance z . w_0 is the beam waist or the radius of the beam when it is at its minimum. z_R is the Rayleigh length. We see in equation 3.5 that the square of the magnitude gives the corresponding gaussian intensity profile. We also see the complex parameter q has a real part that gives the radius of curvature and an imaginary part that gives the gaussian type decay term.

$$\frac{1}{q(z)} = \frac{1}{R(z)} - j \frac{\lambda}{\pi \omega^2(z)} \quad (3.6)$$

$$R(z) = z + z_R^2/z$$

Another important quantity is the divergence of the beam. This is just the beam diameter in the far-field divided by the distance from the beam waist.

$$\theta = \frac{\lambda}{\pi \omega_0}$$

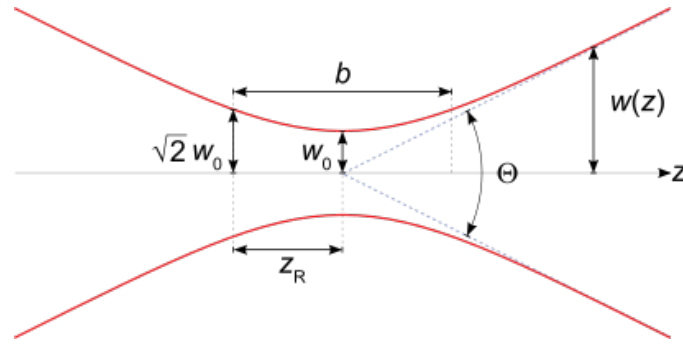


FIGURE 3.2: Gaussian Beam profile cross-section showing the variation of beam spot $w(z)$ [Wiki](#)

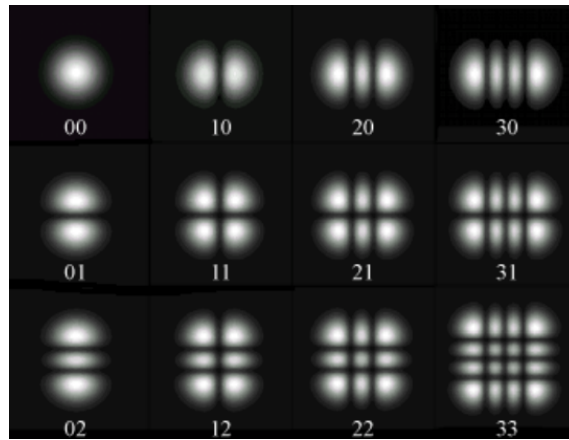


FIGURE 3.3: Rectangular Transverse Modes (TEM(mn)) [\(Wikipedia\)](#)

If we do not impose the azimuthal invariance in the Helmholtz equation, then the solutions take the form of Hermite polynomials ([Svelto](#)). See figure 3.3.

$$E_{mn}(x, y, z) = E_0 \frac{w_0}{w} H_m \left(\frac{\sqrt{2}x}{w} \right) H_n \left(\frac{\sqrt{2}y}{w} \right) \exp[-(x^2 + y^2) \left(\frac{1}{w^2} + \frac{ik}{2R} \right) - ikz - i(m+n+1)\psi]$$

the corresponding intensity pattern is,

$$I_{mn}(x, y, z) = I_0 \left(\frac{w_0}{w} \right)^2 \left[H_m \left(\frac{\sqrt{2}x}{w} \right) \exp \left(\frac{-x^2}{w^2} \right) \right]^2 \left[H_n \left(\frac{\sqrt{2}y}{w} \right) \exp \left(\frac{-y^2}{w^2} \right) \right]^2.$$

3.3 M squared parameter

The M squared parameter is a fundamental metric in laser and optics, quantifying the quality of a laser beam or optical system. It encapsulates beam divergence, size, and shape in a single dimensionless value. The ISO standard 11146 definitions [International Organization for Standardization \(2005\)](#) for the same is,

$$M^2 = \frac{\omega\theta}{\omega_0\theta_0} = \frac{\pi\omega\theta}{\lambda}.$$

The divergence angle (assuming large z) is given by $\theta_0 = \omega(z)/z = \omega_0/z_R = \lambda/(\pi\omega_0)$. The M squared is defined in such a way that if the beam is a pure gaussian then the θ will cancel the remaining factors present in the M squared formula and we get $M^2 = 1$. Assuming a deviation from true gaussian.

$$\omega'^2 = \omega'_0(1 + (z/z'_r)^2)$$

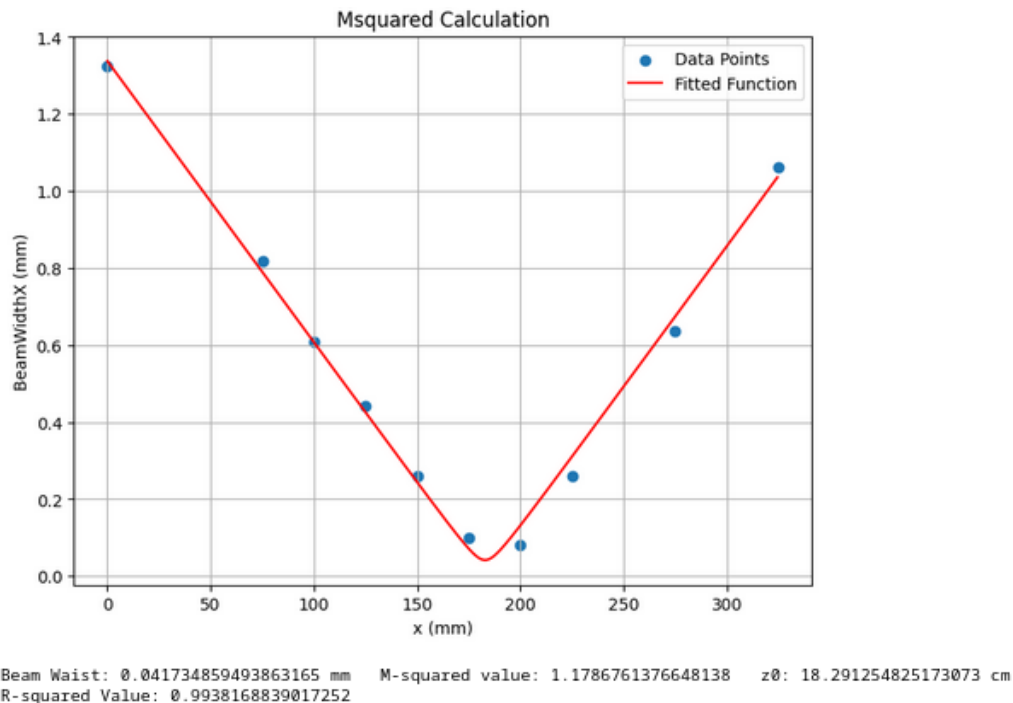
$$\omega'_0\theta' = M^2\omega_0\theta_0, \quad \theta' = \omega'_0/z'_R, \quad 1/z'_R = M^2 \frac{\lambda}{\pi\omega'^2}$$

Which finally gives us the fit formula (dropping the prime superscript),

$$\omega(z)^2 = \omega_0^2 + \left(\frac{z - z_0}{\omega_0} \right)^2 \left(\frac{M^2\lambda}{\pi} \right)^2 \quad (3.7)$$

3.3.1 Observations

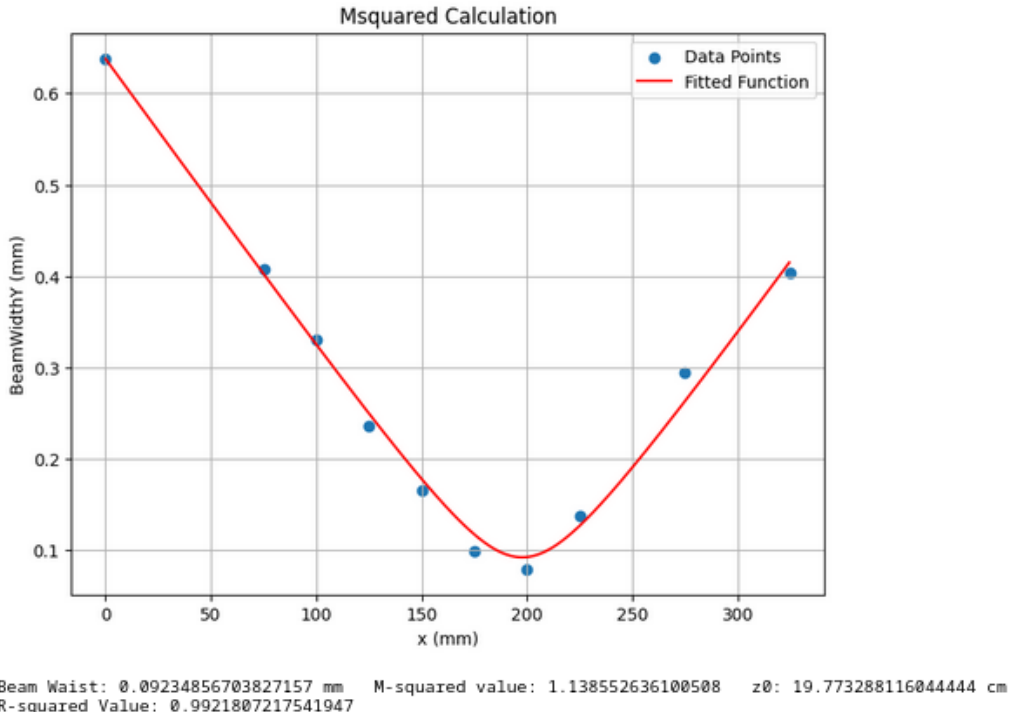
The optical beam in our setup has a minimal divergence, due to which one has to take readings of the beam radius at very large distances. To overcome this a lens of $f = 25.0 \text{ cm}$ is used. The product $\omega\theta$ doesn't change when a beam passes through a lens, this property can be used to find the M^2 value for the beam over a short range,

FIGURE 3.4: M^2 fit in the x-direction

because then the divergence is large giving quick deflection at a short distance. The statistical error in measurement is 0.02 mm (upper bound based on the readout from the camera). After fitting the curve according to equation 3.7, the beam waist was found to be 0.04mm and 0.09mm in the x and y directions respectively. We see a little deviation from the ideal behavior as the $M^2 = 1.18$ in the x-direction and $M^2 = 1.14$ in the y-direction (figure 3.4 and 3.5). But the value is good enough to carry on further experiments.

3.4 The Ray Transfer Matrix Method

The Ray Transfer Matrix (RTM) method is a powerful tool in optics for analyzing the propagation of light through optical systems. It can help in finding resonator stability for lasers and help in finding different parameters during gaussian beam

FIGURE 3.5: M^2 fit in the y-direction

propagation. It employs matrices to describe the transformation of rays as they pass through various optical elements. By cascading these matrices, the RTM method enables efficient and systematic analysis of complex optical systems. Each optical element like lens/free space/dielectric interface in RTM analysis has its representation as a matrix. The ray itself is given by a 2×1 vector. To get the final profile of a ray one just needs to multiply all the matrices and then apply it on the ray vector. The first row of the vector contains the distance from the optical axis. The second row contains the positive angle it subtends with the optical axis. In the figure 3.6 we see a ray (x_1, θ_1) being transformed to (x_2, θ_2) .

$$\begin{bmatrix} x_2 \\ \theta_2 \end{bmatrix} = \begin{bmatrix} A & B \\ C & D \end{bmatrix} \begin{bmatrix} x_1 \\ \theta_1 \end{bmatrix}$$

Where A, B, C, and D are given by,

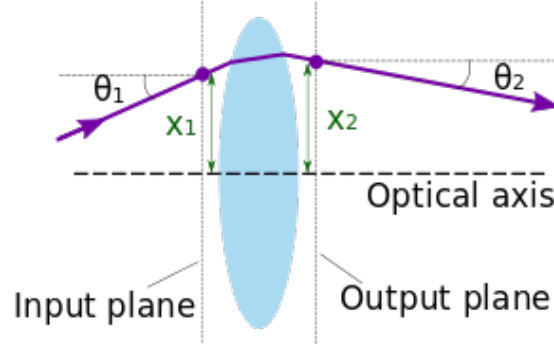


FIGURE 3.6: A ray vector being transformed by an optical element

$$A = \begin{bmatrix} x_2 \\ x_1 \end{bmatrix}_{\theta_1=0}; \quad B = \begin{bmatrix} x_2 \\ \theta_1 \end{bmatrix}_{x_1=0}; \quad C = \begin{bmatrix} \theta_2 \\ x_1 \end{bmatrix}_{\theta_1=0}; \quad D = \begin{bmatrix} \theta_2 \\ \theta_1 \end{bmatrix}_{x_1=0}$$

Here are a few examples of RTMs of some optical elements.

$$\text{Thin lens : } \begin{bmatrix} 1 & 0 \\ -\frac{1}{f} & 1 \end{bmatrix} \quad (3.8)$$

$$\text{Free Space Distance } d : \begin{bmatrix} 1 & d \\ 0 & 1 \end{bmatrix}$$

$$\text{Dielectric Interface : } \begin{bmatrix} 1 & 0 \\ 0 & \frac{n_1}{n_2} \end{bmatrix}$$

RTMs can be used for gaussian beams although the treatment is a little different.

We use the complex beam parameter 'q' defined in equation 3.6. The general form of transformation for any optical element is then given by,

$$q_f = \frac{Aq_i + B}{Cq_i + D} \quad (3.9)$$

where q_i and q_f are the complex beam parameters before and after the optical elements. For example, if we use a thin lens (equation 3.8) then the new complex

parameter becomes.

$$q_f = \frac{q_i}{1 - q_i/f}$$

3.5 Summary of Fiber Optic Physics

Fiber optic cables work on the principle of total internal reflection. The inner core of the fiber has a material of refractive index greater than the outer cladding material. Due to this the angle condition for total internal reflection becomes.

$$\theta > \sin^{-1} \left[\frac{n_{cladding}}{n_{fiber}} \right]$$

The fiber used in this project is a polarization-maintaining fiber.

3.5.1 Polarization Maintaining Fiber

Polarization-maintaining (PM) fibers are a special type of optical fiber designed to maintain the polarization of light as it propagates through the fiber. PM fibers are typically designed with stress-induced birefringence. Stress-induced birefringence occurs when stress is applied to the fiber, which can result from the design of the fiber's core and cladding structure or external mechanical stress applied to the fiber. This stress causes a difference in refractive index for light polarized in two orthogonal directions, effectively creating a fast axis and a slow axis, which maintains the polarization.

3.5.2 Mode Field Diameter

Another important parameter associated with fiber physics is mode field diameter (MFD). MFD is defined as the beam width propagating in a single-mode fiber. The beam width is defined as the point where the beam power becomes $1/e^2$ of the peak power. As a rule of thumb, the beam diameter entering the fiber should be the same as the given mode field diameter in the datasheet of the fiber. This prevents the loss of optical power. To do this we use the RTM method to find the appropriate lens such that the beam after the lens enters the fiber properly.

Chapter 4

Acousto Optic Modulator and PID stabilization setup

4.1 Introduction

This chapter contains the theory and application of the acoustic optic Modulator (AOM). Furthermore, it explores the theory behind signal mixers and their integral role in driving AOMs. Additionally, we investigate the crucial feedback loop involving a Proportional-Integral-Derivative (PID) controller, which is harnessed to ensure the stability of the laser beam's intensity. AOMs working with a PID feedback loop provide control over the laser intensity. Later this stabilized laser beam is supplied to the AOD (Acousto Optic Deflector), which creates the array of beam spots.

4.2 Acousto Optic Modulator

The model of the AOM used in this project is AOM 3080-125 from Gooch and Housego. AOMs work on creating diffraction grating of sinusoidal refractive index in a crystal using radio frequency acoustic waves generated by a transducer attached to the end of the crystal. The crystal used in our AOM is TeO₂ (acoustic velocity 4.2mm/ μ s). In the datasheet, the center frequency is given to be 80 MHz. This will be generated by a signal generator whose output will be supplied to an amplifier which in turn will be connected to the AOM. The maximum (mV_{rms}) of the signal generator amplitude will be decided by the maximum power input allowed for the AOM. This is dependent on the wavelength of the light. The light we use has a wavelength of 813nm.

4.2.1 Theory

AOM can be thought of as operating under the Bragg condition. Where the distance between the slits of the grating can be approximated using the frequency supplied to the AOM and the acoustic velocity inside the crystal. For our case frequency is 80 MHz and the acoustic velocity is 4.2mm/ μ s. Using these we get the wavelength which can be thought of as the slit spacing. The Bragg condition is,

$$2\Lambda \sin(\theta) = m\lambda$$

Λ is the wavelength of the sound. λ is the wavelength of light in vacuum. 'm' is the diffraction order. $\Lambda = v/f = 4200/(80 * 10^{-6})m = 52.5\mu m$. Thus we get(for m=1) the deviation angle(2θ) to be around 0.89° . The light inside the crystal is being diffracted from moving planes this is what differentiates this from Bragg's

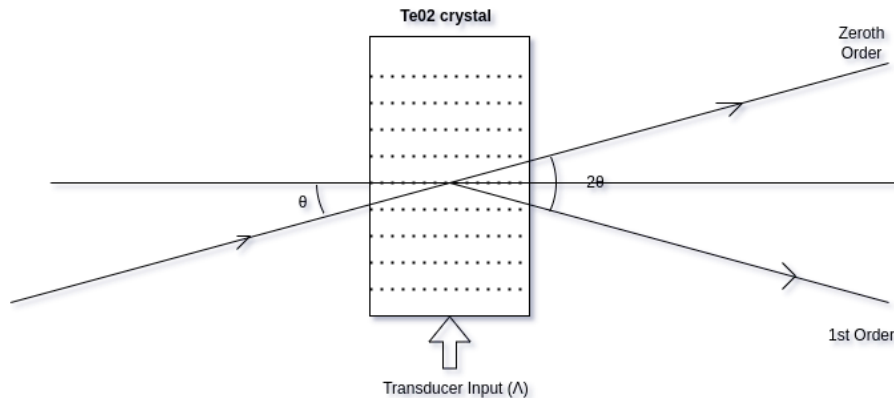


FIGURE 4.1: A rough sketch of AOM

diffraction. One can look at this through phonon-photon scattering. A phonon is absorbed by the incoming light which changes its momentum and energy.

$$\hbar\mathbf{k}_{reflected} = \hbar\mathbf{k}_{incident} + \hbar\mathbf{q}_{phonon} \implies \omega_r = \omega_i + \Omega_{phonon}$$

We see that the absorption of a phonon increases the frequency of the input light. The frequency shift of the light is always in the integer multiple of the sound frequency.

4.2.2 Signal Mixer and Amplifier

A signal mixer or RF mixer is simply a device that takes input of 2 frequencies IF(Intermediate Frequency) and LO(Local Oscillator) and gives an output of the multiplied signal RF(Radio Frequency) see figure 4.2. For example, if the inputs are $A_1 \sin(\omega_1 t)$ and $A_2 \sin(\omega_2 t)$ then the output is $A_1 A_2 \sin(\omega_1 t) \sin(\omega_2 t)$ (in reality, the internal circuit of the mixer generate a superposition of 2 waves as an output. With frequencies of $\omega_1 + \omega_2$ and $\omega_1 - \omega_2$, which, using simple trigonometric expression translates to the expression mentioned before). If the frequency of one of the signals is very low, then that part acts as the enveloping function. For our purpose, we

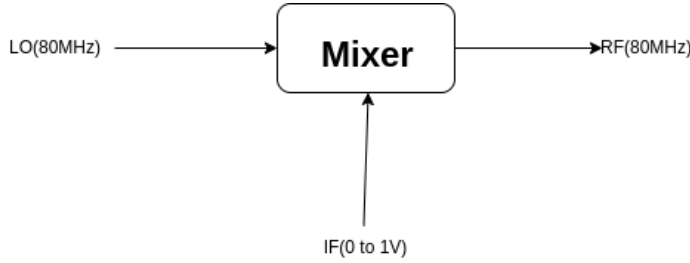


FIGURE 4.2: RF Mixer

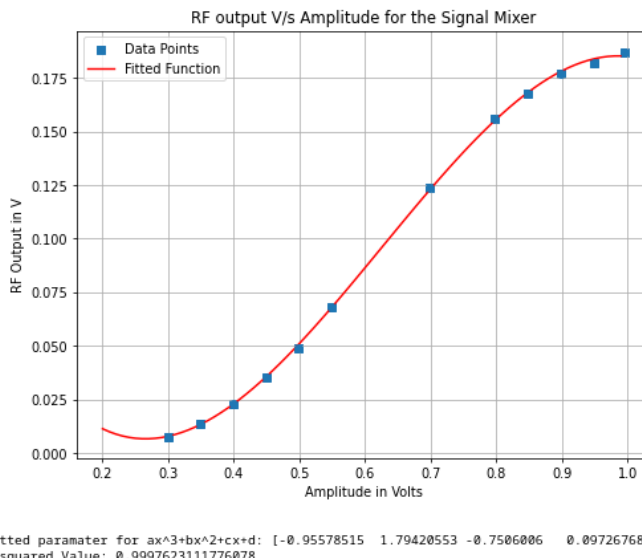


FIGURE 4.3: RF Mixer Characteristic Curve

want to stabilize the intensity of the 1st-order diffracted light from the AOM. Thus we want to get control over the power input to the AOM. To do so our LO becomes the 80 MHz input from the Signal Generator and our control voltage or IF becomes a 0 to 1 Volt output from the QNimble DAQ system. Before that, we must figure out the characteristic curve of our mixer (model ZAD-1H+). The characteristic curve tells us how changing the voltage of the IF changes the output signal, given a particular amplitude and frequency of the input signal. Here the input signal is 80MHz (400mVrms) sinusoid. The output can be seen in the figure 4.3, on the y-axis is the V_{rms} output from the mixer (RF) as measured by the oscilloscope. On the x-axis is the constant DC input from 0 to 1V. Next, we use an amplifier

with a gain of roughly 33 dB (more accurately, the output power is 2406 times the input power), coupled with the mixer to give the final output to the AOM. From the mixer plot it can be seen that the maximum Vrms is around 0.19V. Which for a 50-ohm load corresponds to 0.72mW. When amplified 2406 times this is roughly 1.73W(experimentally it was found at 813nm that the saturation power is roughly 2W, see Figure 4.4).

4.2.3 Diffraction Efficiency

Diffraction efficiency is the ratio of the power of the diffracted light to the power output when the AOM is off. It is a characteristic of AOM that when the input power to the AOM is increased the diffraction efficiency increases and then saturates. So is the case for our model as can be seen in the figure 4.4. One precautionary step is to measure the beam width and confirm if it is smaller than the active aperture of the AOM. While experimenting at first I was not able to get a high diffraction efficiency(saturation at greater than 80 percent) because some part of the beam was being cutoff but later when I used a 3x beam expander in reverse, which gave the 4.4 graph.

The efficiency of the light diffracted is proportional to the acoustic power (P_a), the figure of merit(M_2) of the optical material, electrode geometric factors (L/H), and inversely proportional to the square of the wavelength. The complete relation is given by ([GoochAndHousego](#)),

$$\eta = \sin^2 \left[1.57 \sqrt{\left(\frac{2}{\lambda^2} (L/H) M_2 P_a \right)} \right] \quad (4.1)$$

Equation 4.1 can be simplified to $\eta = \sin^2(a\sqrt{P_a})$. To highlight the dependence of efficiency on the power. Using this relation as the function to fit, the value of the

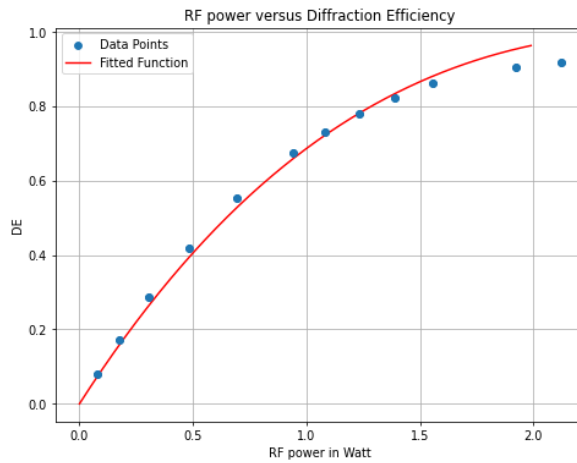


FIGURE 4.4: Diffraction Efficiency Curve

fit parameter for the plot 4.4 turns out to be **a=0.98**, with an R-squared value of 0.99.

4.3 The Optical Setup:

This section contains the complete description of the optical setup shown in the figure. Below are the sequential steps that were followed to build the setup. Refer to figure 4.5.

Step 1: The Toptica Photonics laser that was used initially required to be tuned to 813nm using a wavelength meter.

Step 2: Next a Polarized Beam Splitter (PBS) coupled with a Half Wave Plate, provides a way to control the intensity of the beam. Near the start, a 3x beam expander is also placed. It was realized that the beam size for the AOM was large due to which I was not getting a good diffraction efficiency. Therefore to overcome that a 3x beam expander(reduces the size of the beam roughly 3 times) was used.

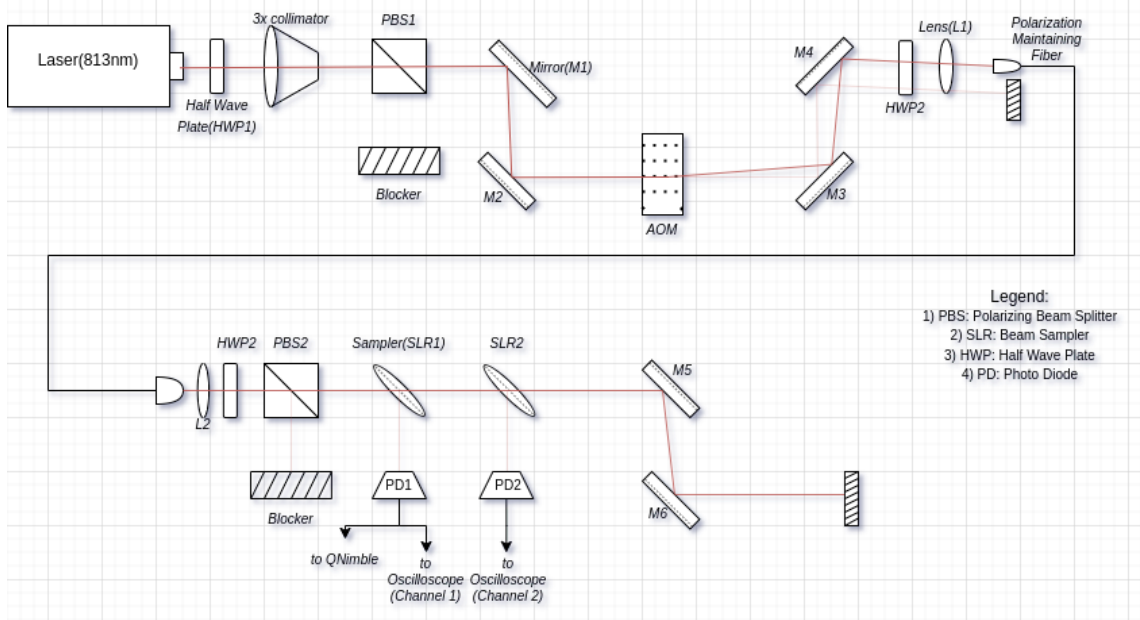


FIGURE 4.5: Optical Setup

Step 3: Then by the help of mirrors M1 and M2, the beam was aligned with the AOM such that the diffraction efficiency is the maximum for 1st order diffracted beam(basically inputting the beam at the Bragg's angle).

Step 4: Mirrors M3 and M4 were used to align the beam into the polarization-maintaining fiber. Here one uses the 'Walking The Beam' technique, to get the maximum laser-fiber coupling efficiency(this is the ratio of input to output laser power in the fiber optic). The use of an appropriate lens is also essential, as mentioned in section 3.4.2, the beam size should match the MFD. This increases the coupling as well as decreases the fluctuation in power output. Getting a good laser-fiber coupling is also essential for the life of fiber. A bad coupling will lead to the dissipation of heat in the fiber which may damage the fiber over time which in turn will decrease the coupling efficiency and the cycle goes on.

Step 5: The output from the fiber is collimated using L2. Then we again have a pair of HWP and PBS, to clean the polarization. The HWP is tuned such that the light falling on the blocker(i.e. one with the horizontal polarization), is minimum.

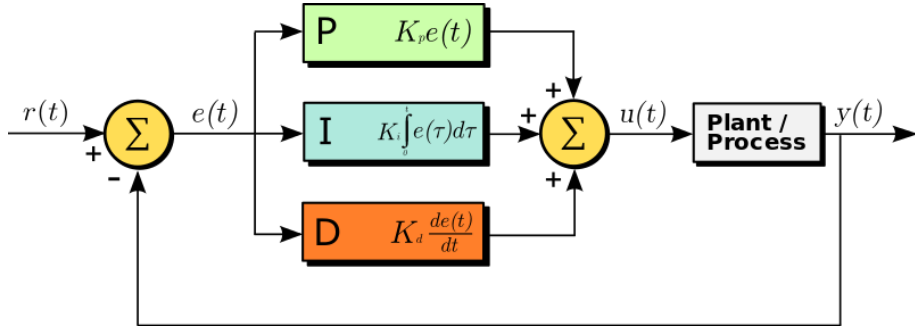


FIGURE 4.6: PID Block Diagram

Step 6: At the right angle, these samplers allow 95% of the light to pass through and sample 5%. SLR1 is used to send the signal to a photodiode(PD1). PD1 is connected to the DAQ system which does the intensity stabilization(section 4.4 contains the stabilization protocol) and also to the Oscilloscope. PD2 is to check if indeed the stabilization is working. The beam after SLR2 goes to the AOD(Acousto Optic Deflector).

4.4 PID (Proportional-Integral-Derivative)

The sampled beam is used as a feedback to stabilize the intensity. PID controller is used to stabilize this.

4.4.1 Theory:

PID control is a widely used feedback control system that plays a crucial role in maintaining the stability and precision of various engineering systems. The acronym PID stands for Proportional, Integral, and Derivative, which represent three distinct components integrated to regulate a system's output based on the difference between a desired setpoint and the actual process variable.

Proportional (P): The proportional component responds to the current error, which is the difference between the setpoint and the actual output. The proportional term contributes to the control signal in proportion to the magnitude of the error. It aims to reduce the steady-state error and bring the system closer to the desired setpoint.

Integral (I): The integral component considers the cumulative effect of past errors over time. It adds a corrective term proportional to the integral of the error, aiming to eliminate any residual steady-state error that may persist despite the proportional control. The integral term is particularly effective in addressing long-term deviations from the setpoint.

Derivative (D): The derivative component anticipates future behavior by considering the rate of change of the error. It adds a corrective term proportional to the rate of change of the error, helping to dampen oscillations and improve system stability. The derivative term is instrumental in reducing overshooting and enhancing the system's transient response.

Mathematical Form: There is a set point variable in time $r(t)$ and we have the processed variable which is $y(t)$. The error variable is $e(t) = y(t) - r(t)$. Our aim is to make the error as less as possible. The Proportional feedback takes the error difference and multiplies a proportional constant K_p to it and sends it for the output. Similarly, the Integral keeps adding the sum of the $e(t)$ in every loop and then multiplies an Integral constant K_i giving it as an output. Similarly the Derivative multiplies a constant K_d and sends it as an output. The complete mathematical

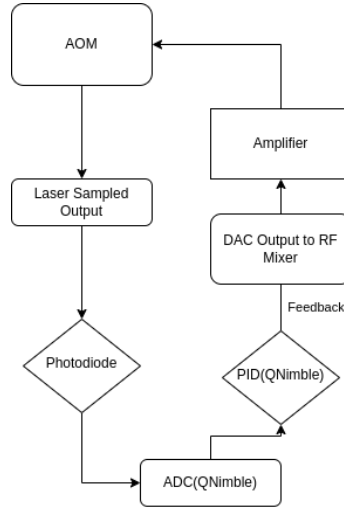


FIGURE 4.7: QNimble PID Flowchart

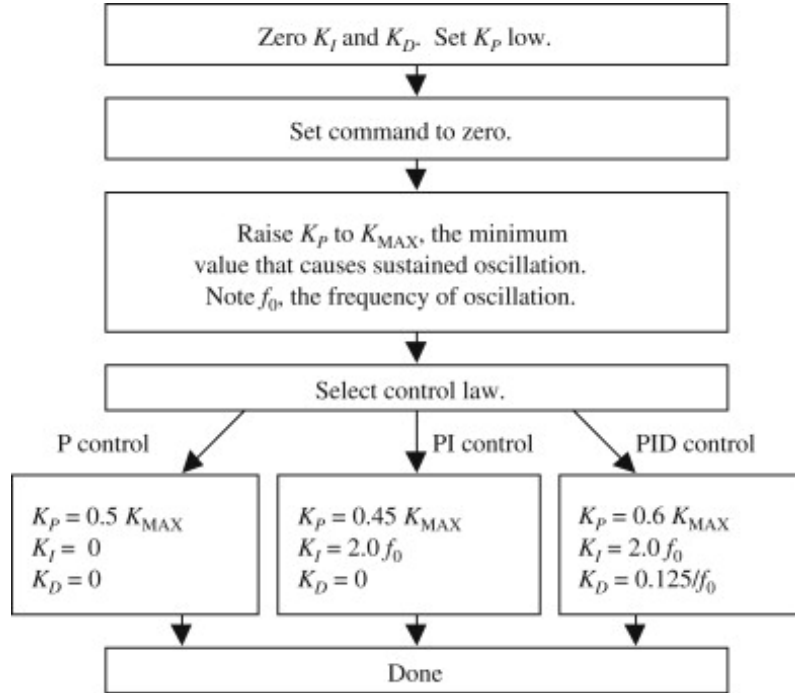
form of the output variable is given as (see figure 4.6),

$$u(t) = K_p e(t) + K_i \int_0^t e(\tau) d\tau + K_d \frac{de(t)}{dt} \quad (4.2)$$

In discretized form, this may be written as,

$$u(t_{k+1}) = K_p e(t_k) + K_i \int_0^{t_k} e(\tau) d\tau + K_d \frac{de(t_k)}{dt} \quad (4.3)$$

The Constants: The PID constants need to be set before uploading the stabilization code. The problem is, what are the optimum parameters? There are multiple ways to find the optimum parameters. Like the Ziegler-Nichols method to optimize the parameters. Figure 4.8 shows the protocol to optimize the PID parameters via Ziegler-Nichols. To quickly get the PID parameters, I start with just K_p slowly increasing it while all other parameters are set to 0. Once I get sustained oscillations, I move to K_i while setting the K_p at roughly half the value of the initial K_p that caused oscillation (I take this as the optimum for K_p). Now I increase the K_i slowly till I start getting sustained oscillations again. Then I take half of the K_i that caused these oscillations as the optimum K_i . To further optimize the parameters, i.e to get

FIGURE 4.8: Ziegler-Nichols Method [Ellis \(2012\)](#)

more near to the optimum parameters I just fine tune near these values.

4.4.2 Implementation:

QNimble Quarto data acquisition system was used to implement PID control for stabilizing the intensity of the AOM's 1st diffracted beam. Figure 4.7 contains a flowchart of the PID stabilization circuit. The QNimble works on Arduino IDE. There are 2 BNC cables attached to PD1, one of them goes to the oscilloscope and the other to the QNimble for feedback. The feedback from PD1 gives an output current that depends on the responsivity curve of the photodiode, this current is then converted to voltage by the ADC high impedance input of QNimble. We need to predefine a set point for the PID code. To find that set point we first supply a nominal voltage(from 0 to 1V) to the RF mixer from the DAC of QNimble. I use 0.8V. This voltage is the 'IF' mentioned in section 4.2.2. The LO is 80MHz(300mVrms)

input from the signal generator. The RF signal after amplification goes to AOM producing the 1st diffracted which enters the fiber. Then the output from the PD1 is seen on channel 1 of the Oscilloscope. The $V_{average}$ of channel 1 (PD1) is noted. This is our setpoint. This setpoint is then written in the code. The Proportional and Integral in the code work to maintain this set point. The Derivative term was not needed as one gets good stability with just Proportional and Integral. The DAC output(of 0 to 1V) from the QNimble will now change according to the fluctuations in the intensity. One side remark, when implementing the PID it was seen that the signal from the feedback photodiode PD1(4.5) was stabilized, however, the signal from the check photodiode i.e. PD2 was unstable. It was later found that the fiber optic was not working well and had been damaged due to which stabilization was not working well.

4.4.3 Results:

The figure 4.9 shows the signal (laser intensity output) at a constant power input to AOM and without any stabilization. The figure 4.10 shows the PID stabilized signal. In figure 4.9 for channel 2 the percentage error (standard deviation/mean) is **0.87%**. After PID stabilization (figure 4.10) for the same channel the percentage error is **0.3%** (the data was taken for two minutes). The K_p and K_i in the code are 1.05 and 0.08 respectively.

Additional noise entering PD1 can cause fluctuation because the PID code will correct for that additional noise which is not coming from the optical setup (e.g. room light). This will lead to an unstable output. In figure 4.10 it can be seen the channel 1 and channel 2 are not completely in sync. This could be due to additional noise entering PD1 or PD2.

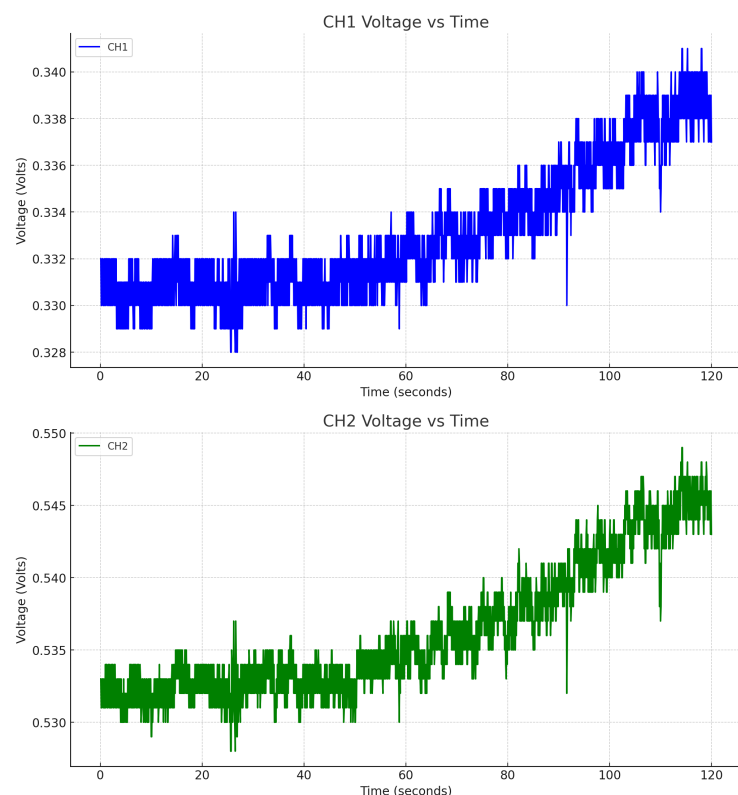


FIGURE 4.9: Output from photodiodes without PID and constant power input in AOM (top one is PD1 output and bottom one is the PD2 output)

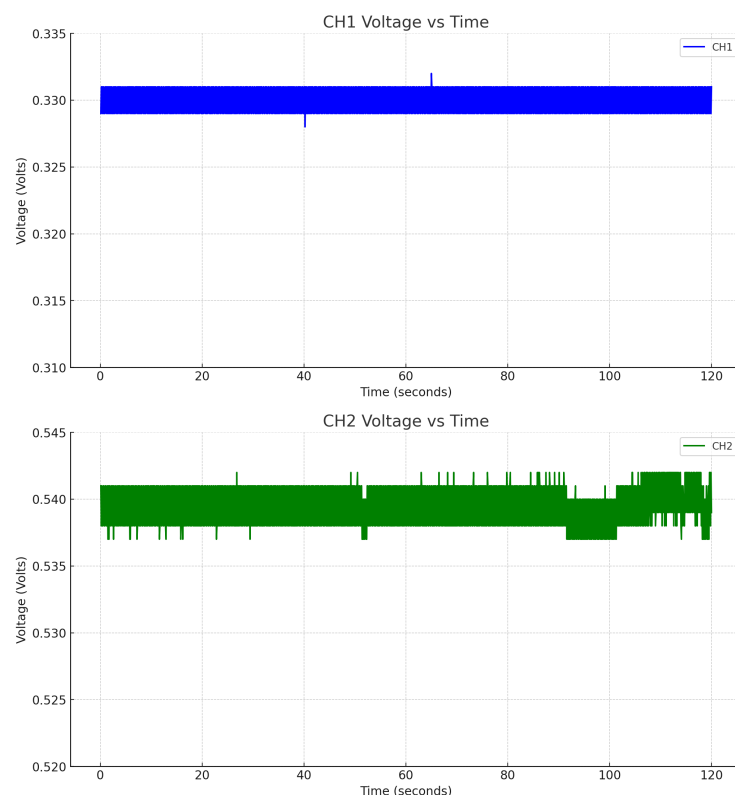


FIGURE 4.10: Output from photodiodes with PID stabilization (top one is PD1 output and bottom one is the PD2 output)

Chapter 5

Acousto-Optic Deflector and High-Frequency Generation using Direct Digital Synthesis

5.1 Introduction

After getting a stabilized output after PID control, an Acousto Optic Deflector (AOD) is placed for the next part of the project. AOD is a device primarily used to deflect the path of a laser beam. The working function is the same as AOM. When an acoustic wave is generated in a crystal or other acousto-optic medium, it creates a periodic modulation of the refractive index. This modulation causes the incident laser beam to be diffracted into different orders, allowing for precise control over the direction of the deflected beam. The difference between the AOM and AOD is that the crystal of AOD is cut and oriented in such a way that the acoustic wave and the incident light interact at an angle that results in efficient deflection

of the light beam. Also, the design of the crystal in AODs is optimized for efficient beam steering and deflection. The maximum number of tweezer traps that can be generated depends on the resolution provided by our AOD. Changing the frequency changes the angle of the laser beam. A fast switch between two frequencies can provide an average potential for two traps. To generate such efficient control over the spectrum of frequencies a Direct Digital Synthesizer (DDS) is used. The Eval board of the DDS IC AD9959 was used. The output from this board is sent to the AOD through an amplifier.

5.2 Characteristics of Acousto-Optic Deflector

In most of the applications, a high resolution is required. Therefore the crystal of AOD is also big (up to 30mm or more ([AAOptoElectronic](#))) which decreases the optical divergence and increases resolution. The resolution is given by,

$$N = \frac{\Delta\Theta}{DIVO}$$

Where $\Delta\Theta$ is the deflection angle range and DIVO is the laser beam divergence. Another important parameter is the Access time $T_a = \phi/V_a$, where ϕ is the beam diameter and V_a is the acoustic velocity. It corresponds to the time for the acoustic wave to travel through the laser beam and thus the necessary time required for the deflector to commute from one position to another. A deflector is often characterized by the time and bandwidth product $T_a \times \Delta F$ (ΔF is the range of frequencies over which the AOD operates). Like AOM the diffraction efficiency for AOD also is controlled by many factors like input angle, RF power, and RF frequency. The operable range of frequencies for the first AOD is from 85.5 MHz to 121.5 MHz ($\Delta F = 36MHz$). The measured beam radius entering AOD was $1.37 \pm 0.02mm$,

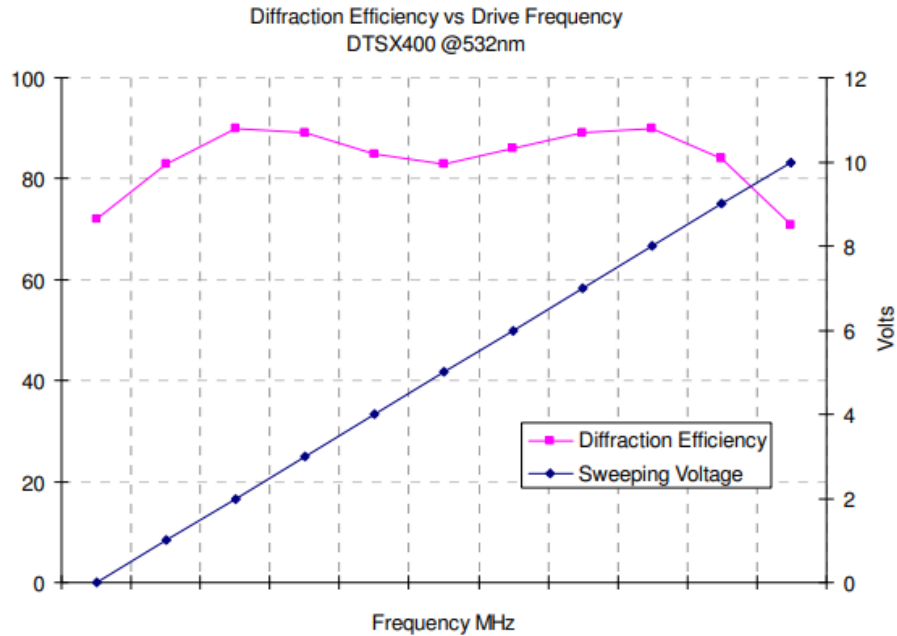


FIGURE 5.1: Diffraction Efficiency vs Frequency from Datasheet

using this and the $V_a = 450m/s$ for TeO_2 crystal, we get,

$$T_a * \Delta F = 75.9$$

From the datasheet of AOD, the characteristic curve for diffraction efficiency versus frequency at 532nm and RF power of 1W, can be seen in figure 5.1.

However, this is not the curve obtained experimentally on the first trial. After some optimization around different frequencies and different input angles, the diffraction efficiency for all the frequencies in the spectrum is increased above 75 percent, and figure 5.1 is reproduced in figure 5.2. The RF power used for figure 5.2 is 1.08W. The RF input for figure 5.2 was given through a signal generator. The optical setup for AOD can be seen in figure 5.7.

The deflected angle from the AOD has a linear relationship with the input frequency as can be seen in figure 5.3. The slope is 1.47 ± 0.03 milliradian/MHz, or 0.084 ± 0.003

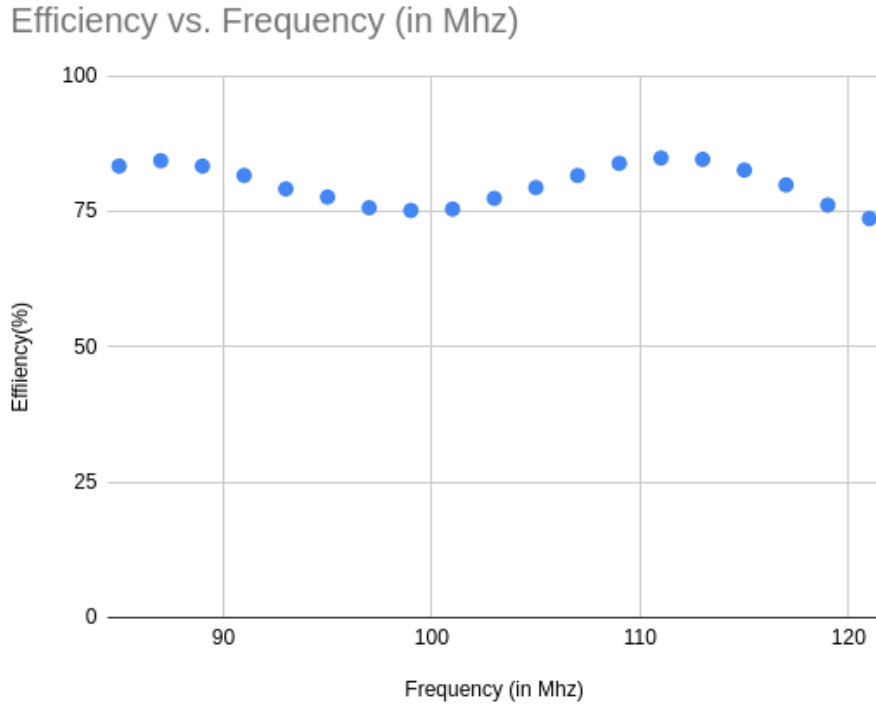


FIGURE 5.2: Diffraction Efficiency versus Frequency

degrees per MHz. This gives a total range of roughly 2.8 degrees for complete frequency bandwidth. The divergence of the beam in the x direction was found to be 0.12 ± 0.02 degrees. The resolution in the x-direction thus comes out to be 23 ± 4 . The divergence of the beam in the y direction was found to be 0.054 ± 0.006 degrees. Thus the resolution in the y-direction comes out to be 52 ± 6 . Thus we see using this setup it is possible to generate greater than 19 tweezer traps in one (x) dimension. The inhomogeneity of the divergence in the two directions may be resolved by using a cylindrical lens.

5.3 Direct Digital Synthesis using AD9959

Direct Digital Synthesis (DDS) is a method that leverages digital data processing modules to generate an output signal with adjustable frequency, amplitude, and

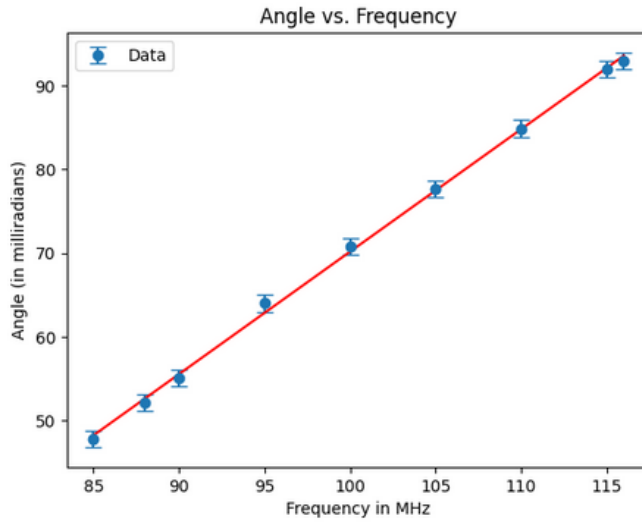


FIGURE 5.3: Diffraction Angle versus Frequency in MHz

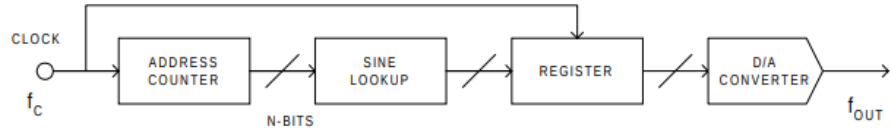


FIGURE 5.4: Flowchart for DDS [Analog Devices](#)

phase, synchronized to a stable clock source. Essentially, the reference clock's frequency is divided in a DDS architecture using a programmable binary tuning word, usually consisting of 24-48 bits. This extensive bit length allows for precise tuning resolution, enhancing the accuracy of the generated output frequency.

5.3.1 Theory of Operation:

A direct digital synthesizer (DDS) can be created using a precise reference clock, an address counter, a programmable read-only memory (PROM), and a digital-to-analog converter (DAC) (figure 5.4). In this setup, the PROM stores digital amplitude information corresponding to a full cycle of a sine wave, essentially functioning as a sine lookup table. The address counter sequentially accesses each memory location in the PROM, retrieving the sine amplitude words, which are then fed into

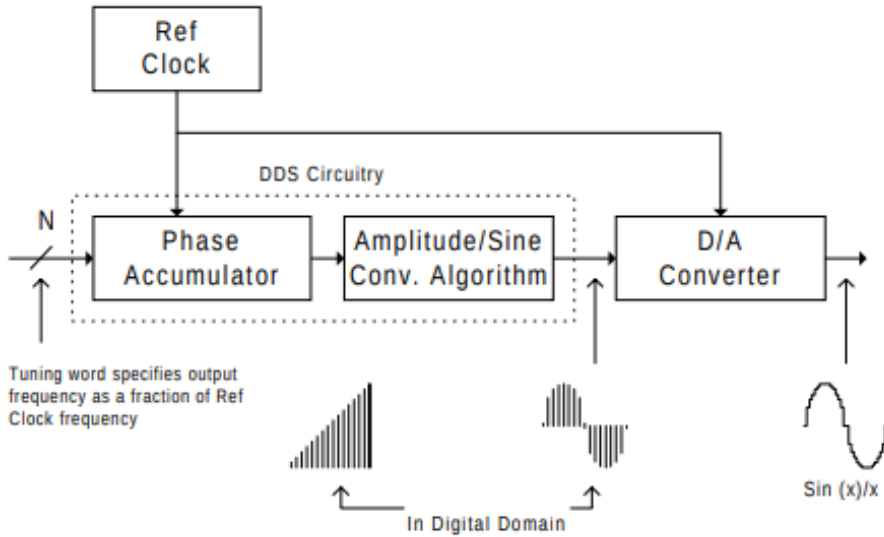


FIGURE 5.5: DDS flowchart with Phase Accumulator [Analog Devices](#)

a high-speed DAC. This converter transforms the digital input into an analog sine wave.

The output frequency of this DDS setup depends on two factors: 1) the frequency of the reference clock and 2) the sine wave step size programmed into the PROM.

When you add a phase accumulator (figure 5.5) function to the digital signal process, it turns into a numerically controlled oscillator, which is a key component of a versatile DDS device. In simple terms, it is like a mechanism that generates a sine wave. In this setup, there's a counter and a phase register before a sine lookup table, replacing an address counter. The phase accumulator acts like a "phase wheel" in the DDS system. Imagine a vector moving around a circle, representing a sine wave cycle. As the vector rotates, it creates the corresponding sine wave output. The phase accumulator mimics the linear rotation of the vector around the phase wheel, and its content corresponds to points on the sine wave cycle. The number of points in this "wheel" is determined by the resolution of the phase accumulator. The output of the phase accumulator is linear and can't directly create a sine wave, only a ramp.

To convert this into a sine wave, a phase-to-amplitude lookup table is used. This table translates the instantaneous output of the phase accumulator into information about the sine wave amplitude, which is then sent to a DAC.

The phase accumulator is a counter that increments its stored number each time it receives a clock-pulse. It increases its stored number each time it gets a clock pulse. The size of the increase is determined by a digital frequency tuning word (ftw) which is added to the overflow of the counter. This word in the delta phase register sets the phase step size between updates based on the reference clock; essentially, it determines how many points to skip around the phase wheel. A larger jump size means the phase accumulator overflows more quickly, completing its equivalent of a sine wave cycle faster. For a 32-bit phase accumulator (which is the default value for AD9959) with N=32, and ftw value of 0000...0001 (one) would cause the phase accumulator to overflow after 2^{32} reference clock cycles. If the M value is changed to 111...11110, the phase accumulator will overflow after only 2^1 clock cycles or two reference clock cycles. This ability to control the jump size is what defines the frequency tuning resolution of the DDS architecture. A simple formula summarising the above description is,

$$f_{out} = \frac{(ftw)(f_s)}{2^N}, \quad (5.1)$$

where f_{out} is the output frequency, f_s is the system clock rate or reference clock frequency and N is the length in bits of the phase accumulator.

5.3.2 Using AD9959 Eval Board with Raspberry Pi Pico

Initially to get RF frequencies a waveform generator was connected to a PC, but the speed of communication was not high enough (40 to 160 Hz). It has been shown by [Huegler et al. \(2023\)](#) that an Agile RF source can be made using AD9959 and

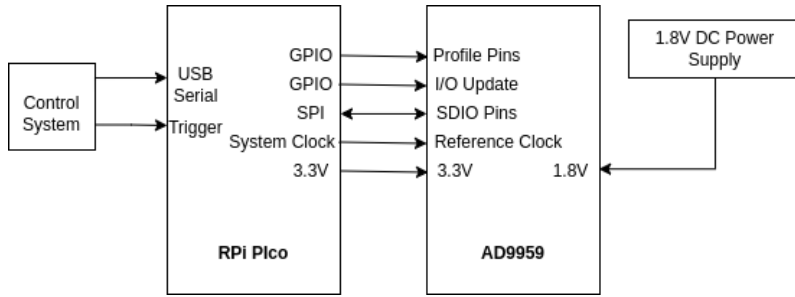


FIGURE 5.6: Block wiring diagram for DDS with RPi Pico (The current drawn by Analog Circuitry of DDS is roughly 0.2 A, when in operation, therefore additional power supply is recommended). More information about the schematic can be found in [Huegler and Meyer \(2023\)](#)

Raspberry Pi Pico (RPi Pico). The firmware for the RPi Pico is written in C and the interface between the PC and RPi is done through Python. The RPi communicates with the DDS board through a Serial Peripheral Interface (SPI). The commands and table can be programmed on RPi and then a serial command from PC can be sent to RPi to run the required tables. Then through SPI communication (which has greater speed), the DDS registers for frequency tuning word and amplitude tuning word is updated. The speed of SPI communication was found to be roughly 54 kilobytes per second. For AD9959 the maximum size for the frequency tuning word and amplitude tuning word is 4 and 3 bytes respectively. Therefore the speed for a combined updation of a frequency and amplitude tuning word ($4+3=7$) is roughly 7 to 8 kHz. The connections between RPi and DDS can be seen in figure 5.6. RPi Pico supplies a 125 MHz system clock to the DDS as its reference clock. With the default PLL (Phase Locked Loop) multiplier set at 4, this results in a DDS system clock of 500 MHz, the maximum supported by the AD9959.

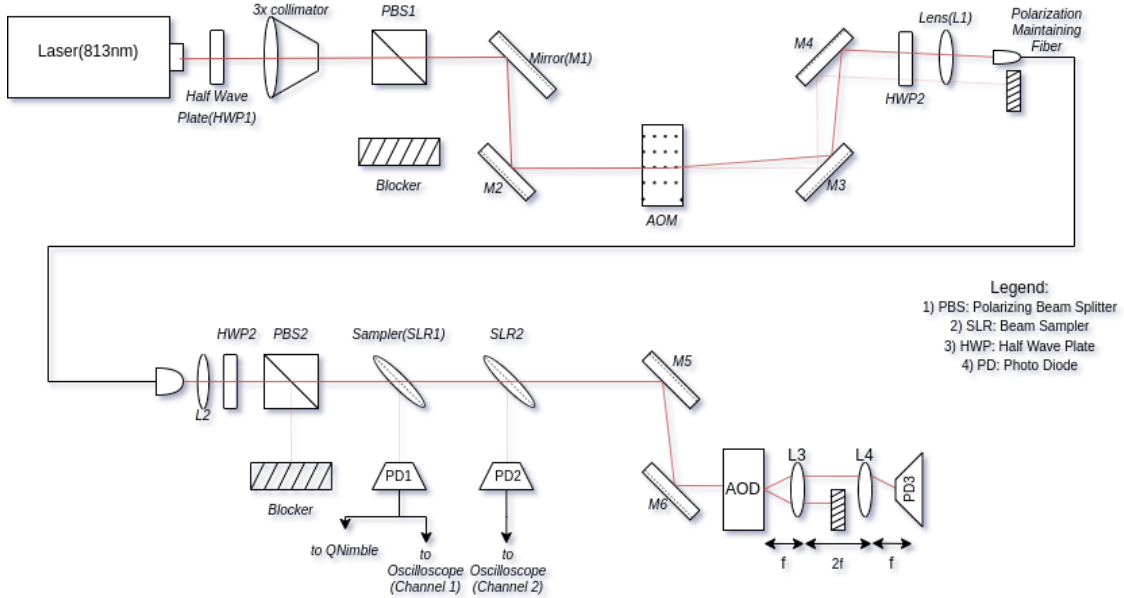


FIGURE 5.7: Optical Setup with AOD in place

5.4 Optical Setup

In chapter 4 the optical setup was shown (figure 4.5) for PID stabilization. The setup is extended, as shown in figure 5.7, for AOD. Two lenses, L3 and L4, of focal length $f=75\text{mm}$ are placed after AOD. The setup focuses all the deflected beams on a single point after L4. This can be seen from RTM analysis easily. The RTM matrix for the setup after AOD is given by,

$$\begin{bmatrix} -1 & 0 \\ 0 & -1 \end{bmatrix}. \quad (5.2)$$

This basically means there is an inversion of the image. The photodiode 'PD3' is aligned accordingly.

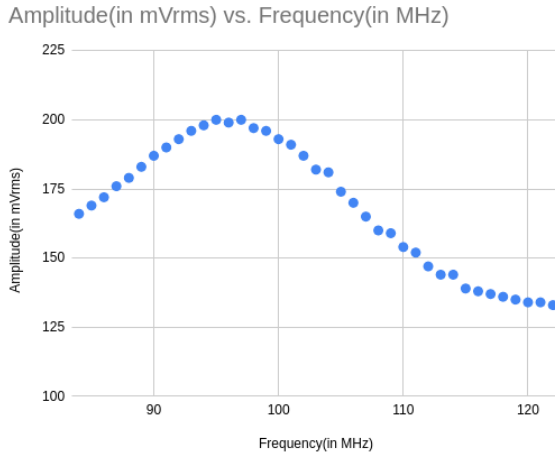


FIGURE 5.8: DDS RF Output Amplitude vs Frequency

5.5 Using DDS with AOD

The next step is to amplify the RF output from DDS and supply it to AOD. Figure 5.8 shows the output of DDS in mVrms as seen on oscilloscope versus frequency. Once the RF power is connected, we can then manually control the frequency output of the DDS thus controlling the deflected angle of the laser beam. Using a 50 ohm terminator it was seen that the amplified RF power does not exceed 0.5W for the amplitude scaling factor set to 1.0 and for all frequencies. Thus it is safe to use the DDS's amplified output with AOD because the maximum allowed RF Power for AOD is 2W.

5.6 Stabilizing the Laser Power Output

We saw that the diffraction efficiency curve for constant power input to AOD is non-linear in figure 5.2, and we also saw a non-linear curve (figure 5.8) for power output from DDS. Therefore when connecting the AOD with the amplified output from DDS and switching between frequencies we expect that the power output of

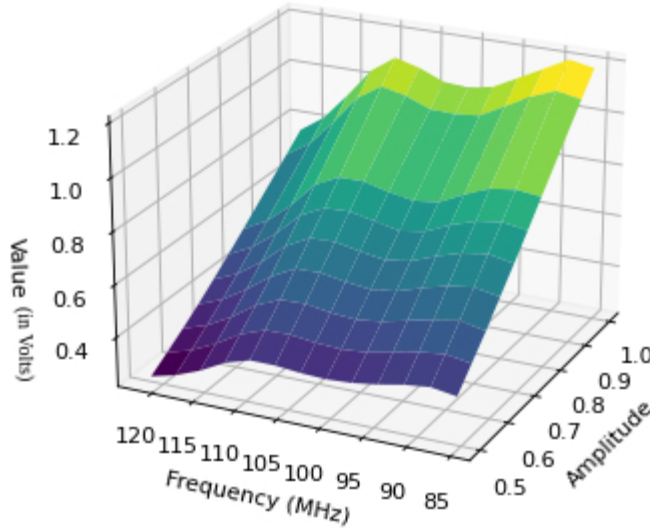


FIGURE 5.9: Plot of 1st Diffracted Beam Power for different Frequencies and Amplitude (the amplitude tuning words have been scaled to values from 0 to 1)

the first-order diffracted beam will vary depending on frequency. To compensate for the change, first I collected data points of first-order diffracted beam power (output from photodiode on Oscilloscope) for different frequencies and amplitudes of DDS output. The heuristic plot is shown in figure 5.9. Now one can find the contour which gives a constant power output. The corresponding pair of frequencies and amplitudes should give a constant power output. Taking the contour for 0.7V plot 5.10 is obtained (the reason for taking this particular value is because this is the output at 120.5 MHz when the amplitude scaling factor reaches its maximum of 1.0).

Figure 5.10 gives us a rough estimate of the list of amplitudes for different frequencies that will produce a constant laser power output. Then by seeing the actual power output when switching over different frequencies, amplitudes are optimized further. The results of stabilization are discussed in the next chapter.

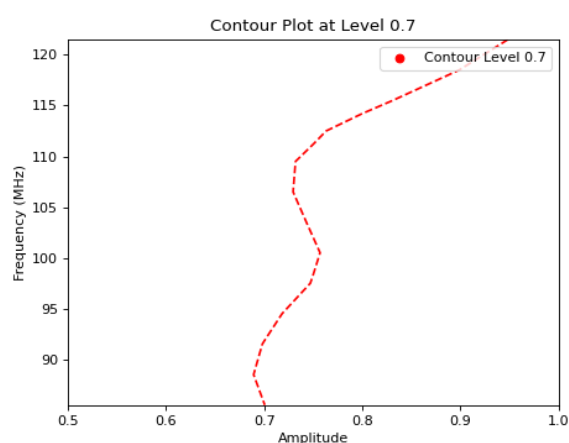


FIGURE 5.10: Contour Plot for Constant Power Output

Chapter 6

Results and Future Prospects

6.1 Summary:

This chapter outlines the results and conclusions of this project, as well as the future prospective. To get a stabilized intensity after AOD a feedback loop comprising of CMOS camera and FPGAs is used [Bluvstein et al. \(2023\)](#). This was not done in this project due to time constraints. However, a table of frequencies and amplitudes was implemented as a proof of concept for stabilized laser beam power output. The power output and the camera images of the same can be seen in this chapter. Later a 2nd AOD was kept after the 1st AOD (in the place of PD3, ref. figure [6.6](#)), and some 2-d patterns were generated.

6.2 1-d Traps:

Figure [6.1](#) contains the image of 6 traps for frequencies of 85.5, 92.5, 99.5, 106.5, 113.5, and 120.5 MHz, covering the complete dynamic range of the AOD and figure

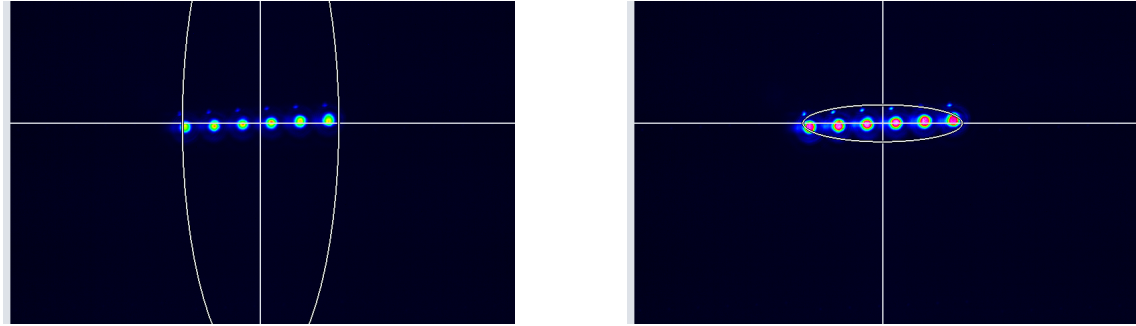


FIGURE 6.1: Six frequencies fast switch output. Exposure time for the first image is 6ms and that for the second one is 12ms



FIGURE 6.2: Cross-Section for figure 6.1

6.2 contains the cross-section for the beam spots shown in figure 6.1. Figure 6.3 shows the power of these traps. Figure 6.4 shows traps for a random sequence of frequencies. The CMOS camera used to take these images is the Gentec Beamage-4M model.

Between each switch of frequencies, the amplitude scaling factor (amplitude tuning word) is set to zero due to which the photodiode output momentarily goes to zero. This creates jumps on the oscilloscope trace. Therefore in the figure 6.3 such jumps have been filtered out. One peculiar behavior observed, as seen in figure 6.3, is that with time the output from AOD destabilizes. This may be due to some thermal effect of AOD. This behavior requires further investigation. The mean value is 0.678V for the first trace and 0.676 for the second one. In the interval of 25 minutes, the standard deviation increased from 0.003V to 0.005V (the standard deviation/average signal*100 increased from 0.49 to 0.68 %).

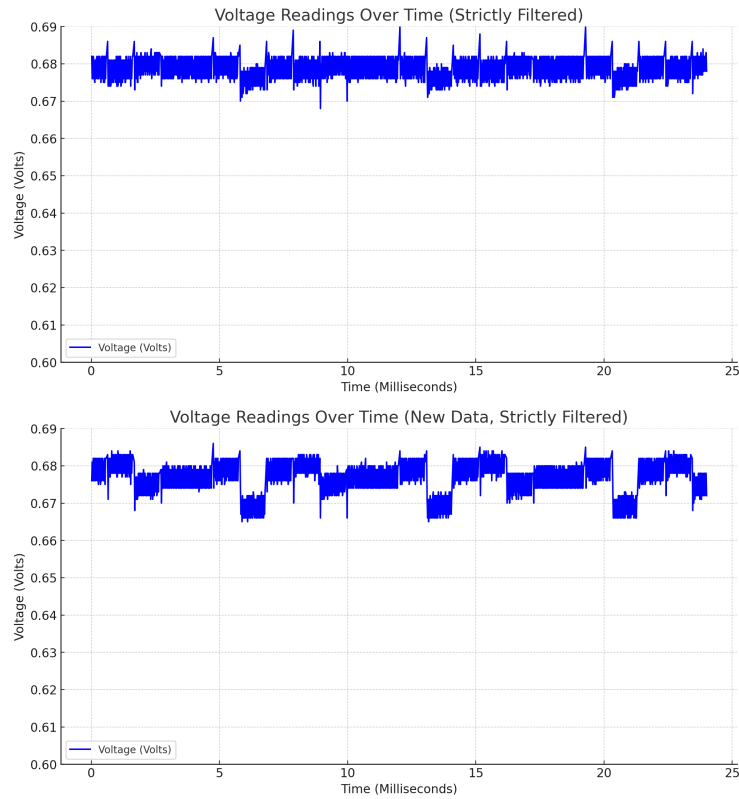


FIGURE 6.3: Output from PD3 (figure 5.7), the two plots were taken 25 minutes apart

6.3 2-d Traps:

To generate 2-d patterns a second AOD must be put after the 1st AOD (figure 6.6), perpendicular to the first AOD to generate deflection in the y direction. Then using a different channel of the DDS the RF input can be sent to this second AOD and we can generate a 2-d pattern. Some of the generated patterns are shown in the figure 6.5. The second AOD still requires some optimization. The minimum Diffraction Efficiency of the second AOD at the time of taking the images is around 45 percent. This needs to be increased to greater than 75 percent as was done for the first AOD. Another problem that needs to be addressed is the stable beam power output from the second AOD. It can be seen in the 2D-generated patterns that some spots are brighter than others. This needs to be addressed.

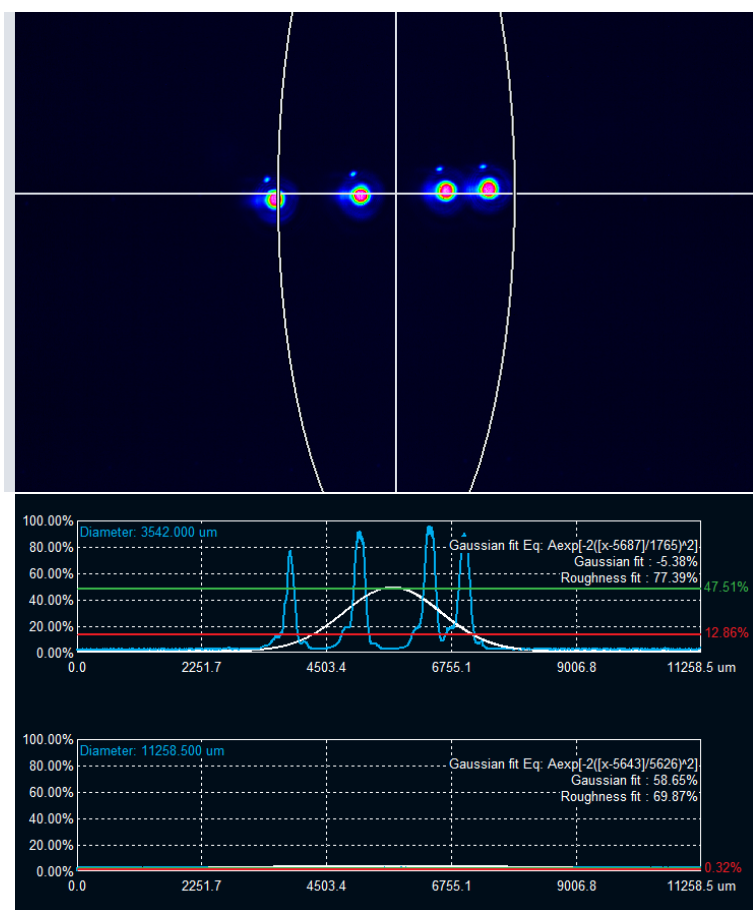


FIGURE 6.4: Random 1-d Pattern

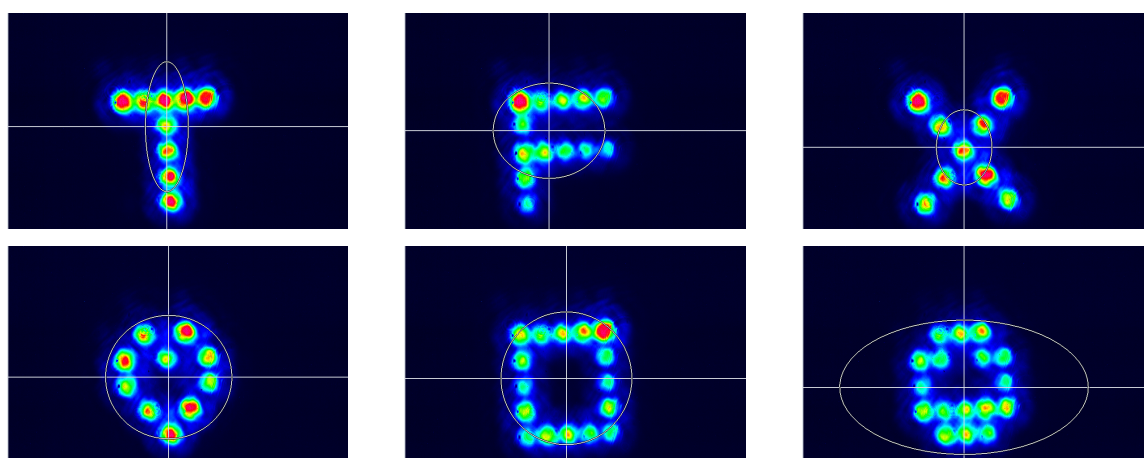


FIGURE 6.5: Some 2-d Patterns generated after the Second AOD

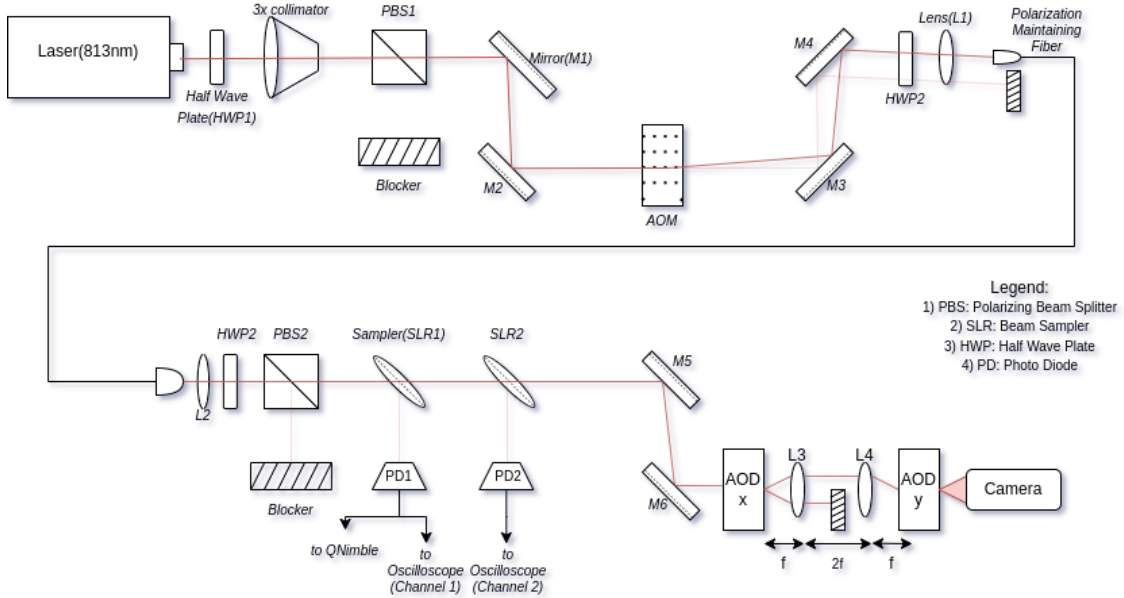


FIGURE 6.6: Optical Setup to generate 2-d Patterns

6.4 Conclusions and Future Prospectives:

In this project, a control system was developed for Strontium tweezer arrays. The purpose was to get precise control over the intensity and position control of beams, with the maximum speed possible. It was found that on average it takes 0.1 to 1 millisecond to switch from one direction to another for the laser beam. The speed constraint is due to the RF generation setup and not due to AOD thus the speed may be increased using a better algorithm and/or a faster SPI communication architecture. Using a table for frequency and amplitude a stable beam intensity profile for six traps was achieved. However, this had some long-term fluctuations which require further investigation. At the end, using a second AOD for movement in the y-direction, some 2-d patterns were formed. This setup requires some additional instruments to enable the trapping of Strontium atoms. One has to employ some laser cooling techniques (e.g. MOT ref. A.0.2) to bring down the temperature of Strontium atoms to a few Kelvins. Then the cloud of Sr atoms can be further cooled

and trapped using the current setup.

Appendix A

Light Matter Interaction and Laser Cooling Techniques

A.0.1 Light Matter Interaction

Light-matter interaction semiclassical is treated by assuming light as an oscillating electric field, then constructing a perturbation Hamiltonian out of it, and then solving it. Detailed derivations for different cases can be found in chapter 7 of [Foot \(2005\)](#). Let's take a 2-level atom with the non-perturbed Hamiltonian to be H_0 , we say the eigenvalues of this to be E_1 and E_2 . The complete wavefunction for the same is given by,

$$|\psi\rangle = c_1|1\rangle e^{-i\omega_1 t} + c_2|2\rangle e^{-i\omega_2 t}. \quad (\text{A.1})$$

Where $\omega_1 = \frac{E_1}{\hbar}$ and $\omega_2 = \frac{E_2}{\hbar}$ and $|1\rangle$ and $|2\rangle$ are the eigenstates. On introducing a perturbation $H_1(t) = e\mathbf{r}\cdot\mathbf{E}_0\cos(\omega t)$, we take the constant c_1 and c_2 to be dependent on time. Thus we have,

$$|\psi\rangle = c_1(t)|1\rangle e^{-i\omega_1 t} + c_2(t)|2\rangle e^{-i\omega_2 t}. \quad (\text{A.2})$$

Next using the time-dependent Schrodinger equation one gets the differential equations for c'_i s,

$$i\dot{c}_1 = \Omega \cos(\omega t) e^{-i\omega_0 t},$$

$$i\dot{c}_2 = \Omega^* \cos(\omega t) e^{i\omega_0 t}.$$

where,

$$\Omega = \frac{\langle 1 | e \mathbf{r} \cdot \mathbf{E}_0 | 2 \rangle}{\hbar} \text{ and } \omega_0 = (E_2 - E_1)/\hbar$$

After some approximations, we find that for monochromatic light, the solutions for c'_i s are,

$$|c_2(t)|^2 = \frac{\Omega^2}{W^2} \sin^2(Wt/2),$$

$$|c_1(t)|^2 = 1 - |c_2(t)|^2.$$

where $W^2 = \Omega^2 + (\omega - \omega_0)^2$. If we take the case of resonance ($\omega = \omega_0$) then,

$$|c_2(t)|^2 = \sin^2(\Omega t/2).$$

We see that $\Omega t = \pi$ has excited all the population. And if we wait a little longer such that $\Omega t = 2\pi$, we see that all population is de-excited. This is the essence of the ' π and $\pi/2$ pulses'. These pulses act as gate operations in Quantum Computing, implementing gates like the X-gate and Hadamard gate. Thus taking suitable levels for Strontium atom one can form a 2-level qubit and thus implement such gate operation by shining the appropriate wavelength of light for appropriate time.

A.0.2 Laser Cooling Techniques

Before using tweezer arrays to confine atoms one has to employ some laser cooling techniques like Zeeman slowing, Sisyphus cooling, and Doppler cooling. In this

appendix, Doppler cooling is described. Doppler cooling exploits the Doppler shift of light to cool a gas of atoms. Atoms moving toward a laser beam see the light as blue-shifted, and those moving away see it as red-shifted. If the laser is slightly red-detuned with respect to the atomic transition of the atom, then the atoms moving in the direction of the laser will absorb the photon and scatter it randomly, thus slowing in the direction of the beam. If 2 counter-propagating beams are used then the atom can be slowed in both directions. If 3 pairs (each for each axis) of laser beams are used then the atom gets slowed down in all directions. Let's take 2 counterpropagating beams and find the force they exert on the atom,

$$F = F_{scattering}((\omega - kv) - \omega_0) - F_{scattering}((\omega + kv) - \omega_0). \quad (\text{A.3})$$

The first term is due to the left propagating beam and the second one is due to the right one. ω is the laser frequency ω_0 is the transition frequency and kv is the Doppler shift due to traveling towards one beam. On solving the above we get,

$$\approx -2 \frac{\partial F}{\partial \omega} kv. \quad (\text{A.4})$$

In the above, we see that the force is similar to a damping force, which slows the atoms. By using the above cooling method one forms an optical molasses where the atoms get clustered at the intersection of the three beams. Next we may put a magnetic field to form, what is called a Magneto-Optical Trap. The setup for the same is shown in the figure A.1. Two current-carrying coils are placed such that a quadrupole magnetic field is developed with zero field strength at the center of the trap. Here the example for $J=1$ ($M_j = +1, 0, -1$) is shown. When the atom moves away from the center it creates zeeman splitting in its energy levels. This leads to the resonance where the laser frequency (ω) matches the energy difference. Following the appropriate selection rules imposed by the beam polarization and magnetic quantum

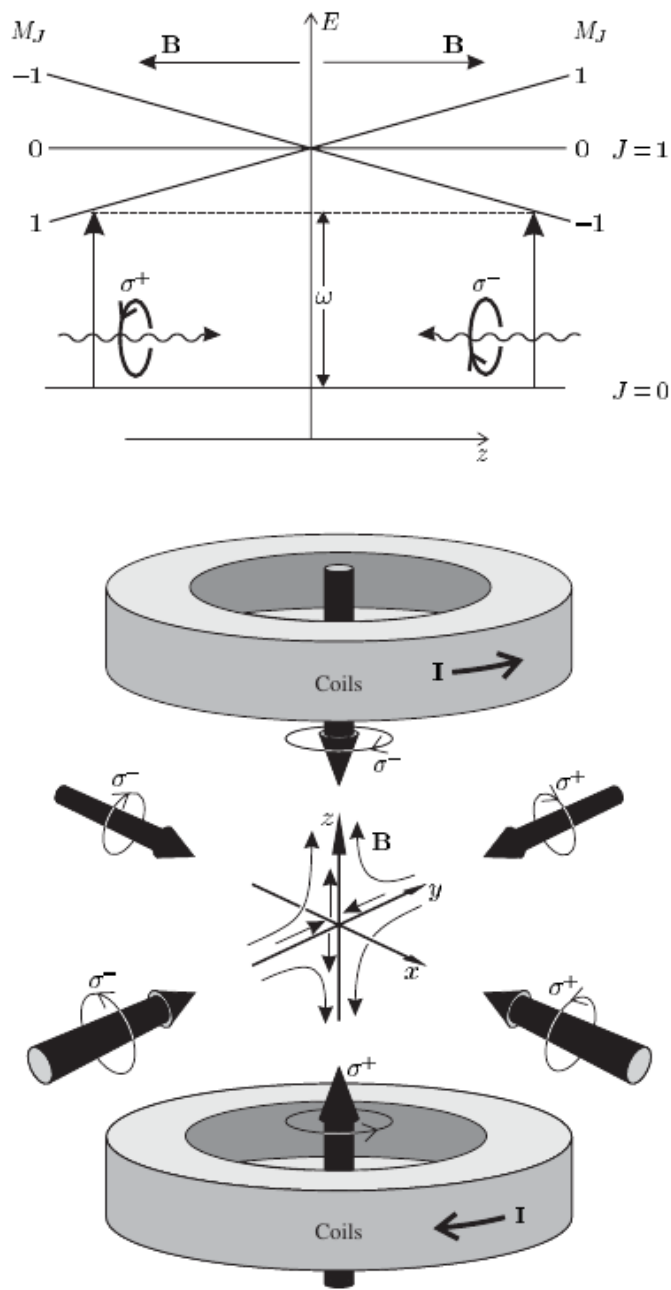
numbers, the photon is absorbed and scattered putting a restoring force when the atom moves away from the center. Assuming the energy level splitting is linear with respect to the distance, we get,

$$\begin{aligned} F_{\text{MOT}} &= F_{\text{scatt}}^{\sigma+}(\omega - kv - (\omega_0 + \beta z)) - F_{\text{scatt}}^{\sigma-}(\omega + kv - (\omega_0 - \beta z)), \\ &\approx -2 \frac{\partial F}{\partial \omega} kv + 2 \frac{\partial F}{\partial \omega_0} \beta z. \end{aligned} \quad (\text{A.5})$$

where $\beta = (g\mu_B/\hbar)\partial_z Bz$, since 'F' only depends on detuning $(\omega - \omega_0)$, we get the final expression,

$$F_{\text{MOT}} = -2 \frac{\partial F}{\partial \omega} (kv + \beta z) = -\alpha v - \frac{\alpha \beta}{k} z. \quad (\text{A.6})$$

The addition of a magnetic field leads to positional dependence. A spring-type force acts on the atoms confining them to the center. MOTs are very robust in the sense that the traps can be loaded directly from room temperature.

FIGURE A.1: Magneto Optical Trap Setup [Foot \(2005\)](#)

Appendix B

Optical Elements Description

B.1 Half-Wave Plate

The half-wave plate (HWP) is an optical device that alters the polarization state of light. In quantum mechanics, the polarization state of a photon is represented by a two-level quantum system, analogous to the spin- $\frac{1}{2}$ system in quantum mechanics. The states $|H\rangle$ and $|V\rangle$ represent horizontal and vertical polarizations, respectively.

A HWP introduces a phase shift of π between these two polarization components, effectively rotating the polarization state by an angle that depends on the orientation of the HWP. The Jones matrix for a HWP with its fast axis at an angle θ with respect to the horizontal is given by:

$$J_{\text{HWP}}(\theta) = \begin{pmatrix} \cos(2\theta) & \sin(2\theta) \\ \sin(2\theta) & -\cos(2\theta) \end{pmatrix}. \quad (\text{B.1})$$

If we take H and V as unit vectors the transformation can be easily described by jones matrix.

B.2 Action of a Quarter-Wave Plate

A quarter-wave plate (QWP) is an optical device that converts linear polarization into circular polarization and vice versa. It introduces a phase difference of $\frac{\pi}{2}$ between the horizontal and vertical components of the polarization state of a photon. The Jones matrix for a QWP oriented at an angle θ with respect to the horizontal polarization is given by:

$$J_{\text{QWP}}(\theta) = \frac{1}{\sqrt{2}} \begin{pmatrix} 1 & -i \cdot e^{-2i\theta} \\ -i \cdot e^{2i\theta} & 1 \end{pmatrix}. \quad (\text{B.2})$$

When a photon with a linear polarization state $|H\rangle$ or $|V\rangle$ passes through a QWP at an angle of $\pi/4$, the polarization state is transformed into a superposition of $|H\rangle$ and $|V\rangle$ with a relative phase of $\pm\frac{\pi}{2}$, resulting in circular polarization.

B.3 Interaction with a Polarizing Beam Splitter

A polarizing beam splitter (PBS) transmits one linear polarization component and reflects the other. A PBS can be represented as a quantum mechanical operator that projects the polarization state onto the horizontal or vertical polarization basis. The action of a PBS can be described by:

$$\hat{P}_{\text{PBS}}|H\rangle = |H\rangle, \quad \hat{P}_{\text{PBS}}|V\rangle = 0, \quad (\text{B.3})$$

for the transmitted horizontal component, and

$$\hat{P}_{\text{PBS}}|V\rangle = |V\rangle, \quad \hat{P}_{\text{PBS}}|H\rangle = 0, \quad (\text{B.4})$$

for the reflected vertical component.

B.4 Ray Transfer Matrix of a Thin Lens

The behavior of light as it passes through a thin lens can be described using ray transfer matrices. The matrix for a thin lens is derived by considering the refraction of light rays at curved surfaces and then combining two such surfaces to model the lens. Using Snell's law on a curved surface one can find the ray transfer matrix for a single surface M_{surface} which is:

$$M_{\text{surface}} = \begin{pmatrix} 1 & 0 \\ \frac{n-n'}{R} & \frac{n}{n'} \end{pmatrix}. \quad (\text{B.5})$$

where n and n' are the refractive indices of the medium before and after the surface, respectively. R is the radius of curvature of the surface. A thin lens can be thought of as two such refractive surfaces put together with their curved sides facing each other. If the separation between the surfaces is negligibly small, we can approximate the lens as a single refractive element with the combined effect of both surfaces. The matrix for the lens, M_{lens} , is then the product of the matrices for each surface:

$$M_{\text{lens}} = M_{\text{surface1}} \cdot M_{\text{surface2}}. \quad (\text{B.6})$$

Assuming the lens is in air ($n = 1$) and the refractive index inside the lens is n' , the matrices for the two surfaces with radii R_1 and R_2 are:

$$M_{\text{surface1}} = \begin{pmatrix} 1 & 0 \\ \frac{1-n'}{R_1} & 1 \end{pmatrix}, \quad M_{\text{surface2}} = \begin{pmatrix} 1 & 0 \\ \frac{n'-1}{R_2} & 1 \end{pmatrix}. \quad (\text{B.7})$$

Multiplying these matrices and assuming the thin lens approximation, we obtain:

$$M_{\text{lens}} = \begin{pmatrix} 1 & 0 \\ \left(\frac{1-n'}{R_1} + \frac{n'-1}{R_2}\right) & 1 \end{pmatrix}. \quad (\text{B.8})$$

The focal length f of the lens is related to the radii of curvature and the refractive index by the lensmaker's formula:

$$\frac{1}{f} = (n' - 1) \left(\frac{1}{R_1} - \frac{1}{R_2} \right). \quad (\text{B.9})$$

Substituting into the matrix, we get the final form of the ray transfer matrix for a thin lens in air:

$$M_{\text{lens}} = \begin{pmatrix} 1 & 0 \\ -\frac{1}{f} & 1 \end{pmatrix}. \quad (\text{B.10})$$

This matrix can be used to analyze the path of rays through a lens and by extension, complex optical systems composed of multiple lenses and other optical elements.

References

- AAOptoElectronic, . aaoptoelectronic.com. <http://www.aaoptoelectronic.com/wp-content/uploads/documents/AAOPTO-Theory2013-4.pdf>. [Accessed 06-12-2023].
- Analog Devices, . A technical tutorial on digital signal synthesis. <https://www.ieee.li/pdf/essay/dds.pdf>. [Accessed 06-12-2023].
- Barredo, D., de Léséleuc, S., Lienhard, V., Lahaye, T., Browaeys, A., 2016. An atom-by-atom assembler of defect-free arbitrary two-dimensional atomic arrays. Science 354, 1021–1023. URL: <http://dx.doi.org/10.1126/science.aah3778>, doi:[10.1126/science.aah3778](https://doi.org/10.1126/science.aah3778).
- Bluvstein, D., Evered, S.J., Geim, A.A., Li, S.H., Zhou, H., Manovitz, T., Ebadi, S., Cain, M., Kalinowski, M., Hangleiter, D., Ataides, J.P.B., Maskara, N., Cong, I., Gao, X., Rodriguez, P.S., Karolyshyn, T., Semeghini, G., Gullans, M.J., Greiner, M., Vuletić, V., Lukin, M.D., 2023. Logical quantum processor based on reconfigurable atom arrays. Nature URL: <https://doi.org/10.1038/s41586-023-06927-3>, doi:[10.1038/s41586-023-06927-3](https://doi.org/10.1038/s41586-023-06927-3).
- Boyd, M.M., 2007. High precision spectroscopy of strontium in an optical lattice: Towards a new standard for frequency and time. Ph.D. thesis. University of Colorado, Boulder.

- Ellis, G., 2012. Chapter 6 - four types of controllers, in: Ellis, G. (Ed.), Control System Design Guide (Fourth Edition). fourth edition ed.. Butterworth-Heinemann, Boston, pp. 97–119. URL: <https://www.sciencedirect.com/science/article/pii/B9780123859204000060>, doi:<https://doi.org/10.1016/B978-0-12-385920-4.00006-0>.
- Foot, C., 2005. Atomic Physics. Oxford Master Series in Physics, OUP Oxford. URL: https://books.google.co.jp/books?id=_CoSDAAAQBAJ.
- GoochAndHousego, . URL: <https://www.optoscience.com/maker/gooch/pdf/IntroductionA0.pdf>.
- Grimm, R., Weidemüller, M., Ovchinnikov, Y.B., 2000. Optical dipole traps for neutral atoms 42, 95–170. URL: <https://www.sciencedirect.com/science/article/pii/S1049250X0860186X>, doi:[https://doi.org/10.1016/S1049-250X\(08\)60186-X](https://doi.org/10.1016/S1049-250X(08)60186-X).
- HANLEY, R., 2018. Creation of a strontium microtrap: Towards a spin-squeezed atomic clock. URL: <http://etheses.dur.ac.uk/12905/>.
- Huegler, E., Hill, J.C., Meyer, D.H., 2023. An agile radio-frequency source using internal linear sweeps of a direct digital synthesizer. Review of Scientific Instruments 94. URL: <http://dx.doi.org/10.1063/5.0163342>, doi:<10.1063/5.0163342>.
- Huegler, E., Meyer, D., 2023. dds-sweeper. <https://github.com/QTC-UMD/dds-sweeper>.
- International Organization for Standardization, 2005. Lasers and laser-related equipment – Test methods for laser beam widths, divergence angles and beam propagation ratios. ISO Standard ISO 11146. International Organization for Standardization.

Svelto, O., . Principles of lasers. URL: <https://link.springer.com/book/10.1007/978-1-4419-1302-9>.

Takamoto, M., Katori, H., 2003. Spectroscopy of the $^1s_0 - ^3p_0$ clock transition of ^{87}Sr in an optical lattice. Phys. Rev. Lett. 91, 223001. URL: <https://link.aps.org/doi/10.1103/PhysRevLett.91.223001>, doi:10.1103/PhysRevLett.91.223001.

Wiki, . URL: https://en.wikipedia.org/wiki/Gaussian_beam#/media/File:GaussianBeamWaist.svg.

Wikipedia, . File:Hermite-gaussian.png - Wikimedia Commons — commons.wikimedia.org. <https://commons.wikimedia.org/wiki/File:Hermite-gaussian.png>.